



**HAL**  
open science

# Simulating Longitudinal Brain MRIs with known Volume Changes and Realistic Variations in Image Intensity

Bishesh Khanal, Nicholas Ayache, Xavier Pennec

► **To cite this version:**

Bishesh Khanal, Nicholas Ayache, Xavier Pennec. Simulating Longitudinal Brain MRIs with known Volume Changes and Realistic Variations in Image Intensity. *Frontiers in Neuroscience*, 2017, 10.3389/fnins.2017.00132 . hal-01348959v2

**HAL Id: hal-01348959**

**<https://inria.hal.science/hal-01348959v2>**

Submitted on 7 Feb 2017 (v2), last revised 22 Mar 2017 (v3)

**HAL** is a multi-disciplinary open access archive for the deposit and dissemination of scientific research documents, whether they are published or not. The documents may come from teaching and research institutions in France or abroad, or from public or private research centers.

L'archive ouverte pluridisciplinaire **HAL**, est destinée au dépôt et à la diffusion de documents scientifiques de niveau recherche, publiés ou non, émanant des établissements d'enseignement et de recherche français ou étrangers, des laboratoires publics ou privés.

---

# Simulating Longitudinal Brain MRIs with known Volume Changes and Realistic Variations in Image Intensity

**Bishesh Khanal, Nicholas Ayache, and Xavier Pennec**

*Asclepios, INRIA Sophia Antipolis Méditerranée, Sophia Antipolis, France*

Correspondence\*:

Bishesh Khanal

bishesh.khanal@inria.fr

## 2 ABSTRACT

3 This paper presents a simulator tool that can simulate large databases of visually realistic  
4 longitudinal MRIs with known volume changes. The simulator is based on a previously proposed  
5 biophysical model of brain deformation due to atrophy in AD. In this work, we propose a novel  
6 way of reproducing realistic intensity variation in longitudinal brain MRIs, which is inspired by an  
7 approach used for the generation of synthetic cardiac sequence images. This approach combines  
8 a deformation field obtained from the biophysical model with a deformation field obtained by a  
9 non-rigid registration of two images. The combined deformation field is then used to simulate a  
10 new image with specified atrophy from the first image, but with the intensity characteristics of the  
11 second image. This allows to generate the realistic variations present in real longitudinal time-  
12 series of images, such as the independence of noise between two acquisitions and the potential  
13 presence of variable acquisition artifacts. Various options available in the simulator software are  
14 briefly explained in this paper. In addition, the software is released as an open-source repository.  
15 The availability of the software allows researchers to produce tailored databases of images with  
16 ground truth volume changes; we believe this will help developing more robust brain morphometry  
17 tools. Additionally, we believe that the scientific community can also use the software to further  
18 experiment with the proposed model, and add more complex models of brain deformation and  
19 atrophy generation.

20 **Keywords:** Neurodegeneration, biophysical modelling, biomechanical simulation, simulated database, synthetic images, synthetic  
21 longitudinal MRIs

## 1 INTRODUCTION

22 Structural Magnetic Resonance Imaging (MRI) has been widely used for in-vivo observation of  
23 morphological changes over time in human brain. Atrophy or tissue volume loss measure from structural  
24 MRI is an established biomarker for neurodegeneration (Frisoni et al., 2010). There is a large number of  
25 brain morphometry algorithms developed in the literature which estimate global or local atrophy from  
26 structural MRIs (Wright et al., 1995; Freeborough and Fox, 1997; Ashburner and Friston, 2000; Smith et al.,

27 2002; Hua et al., 2008). Volume/atrophy measurements obtained from such algorithms have been used to  
28 test various clinical hypotheses about neurodegenerative diseases (Wright et al., 1995; Sepulcre et al., 2006;  
29 Koch et al., 2016). Similarly, comparison of different neurodegenerative diseases have also been performed  
30 based on these measurements (Rosen et al., 2002; Whitwell and Jack Jr, 2005). Since atrophy estimation is  
31 an inverse problem, the estimation algorithms require a model with certain parameters. The results obtained  
32 from such algorithms depend on model assumptions and the parameters used. Often, these assumptions  
33 are implicit and cannot be directly linked to the biophysical process of neurodegeneration. For instance,  
34 tensor based morphometry (TBM) encodes local volume changes by computing Jacobian determinants of  
35 the deformation field obtained from non-linear registration of longitudinal MRIs (Ashburner and Ridgway,  
36 2015). Such methods contain model biases because TBM results depend on the choices of regularization  
37 used during the registration of images (Ashburner, 2013). Likewise, edge-based methods such as BSI,  
38 SIENA etc. are sensitive to unmatched image contrasts between scans, poor signal-to-noise ratio, partial  
39 volume effects, segmentation errors etc. (Preboske et al., 2006; Prados et al., 2015). Estimating and  
40 correcting the bias present in such morphometry tools is important, especially for clinical applications.

41 In addition to tracking volumetric changes in specific brain structures, longitudinal imaging data can also  
42 be used to study the temporal inter-relationship of atrophy in different structures. For instance, Carmichael  
43 et al. (2013) studied the groupings of 34 cortical regions and hippocampi from the per-individual rates of  
44 atrophy estimates in these regions. In Fonteijn et al. (2012), authors defined AD progression as a series  
45 of discrete events. Along with other clinical events, the timings of atrophy in various brain structures  
46 were included in a set of discrete events. Without any prior to their ordering, the model finds the most  
47 probable order for these events from the data itself. They used Bayesian statistical algorithms for fitting the  
48 event-based disease progression model. The objective of these studies were to understand how different  
49 regions of brain evolve during the neurodegeneration.

50 In this context of increasing use of the atrophy measurements from longitudinal MRIs in testing or  
51 discovering clinically relevant hypotheses, it is important to study the bias and variability of the atrophy  
52 estimation algorithms. The actual volume changes in real longitudinal MRIs are not known. Thus, the  
53 evaluation and validation of atrophy estimation algorithms require generating images with known volume  
54 changes, called ground truth images.

55 A number of atrophy simulators have been proposed in the literature to produce ground truth MRIs  
56 (Smith et al., 2003; Camara et al., 2006; Karaçali and Davatzikos, 2006; Pieperhoff et al., 2008; Sharma  
57 et al., 2010; Modat et al., 2014; Radua et al., 2014; Khanal et al., 2016b). Most of these simulators use a  
58 model that attempts to produce a deformation field with the specified volume changes in the input brain  
59 MRI. To produce realistic scenarios of noise and acquisition artifacts, some of these simulators also use a  
60 model to produce noise and artifacts in the simulated image.

61 Such simulators have been used for the validation of registration or segmentation based atrophy estimation  
62 algorithms (Camara et al., 2008; Pieperhoff et al., 2008; Sharma et al., 2010), to estimate the bias in such  
63 algorithms, and also to estimate uncertainty in the measured atrophy (Sharma et al., 2013). These studies  
64 have estimated the bias by simulating simple atrophy patterns in a small number of brain regions, or  
65 uniform diffused global atrophies. However, real case scenarios could have a much more complex atrophy  
66 distribution occurring in many brain structures at the same time.

67 Noise and imaging artifacts have an important impact on the results obtained from atrophy estimation  
68 algorithms (Pieperhoff et al., 2008; Camara et al., 2008; Sharma et al., 2010). Thus, proper evaluation  
69 of atrophy estimation algorithms by using simulated ground truth images requires simulation of realistic

70 variation in noise and intensity too. All the previous atrophy simulators have warped the input baseline  
71 image with the deformation field obtained from a model of brain deformation. Then, extra noise and  
72 artifacts are added on this warped image by using another artificial model. The intensity noise in structural  
73 MRIs has been shown to be governed by a Rician distribution where the noise is Gaussian in k-space  
74 (Gudbjartsson and Patz, 1995). Thus the Rician noise can be added in the simulated images as follows:

- 75 • Use two independent random variables following zero-mean Gaussian distribution to compute the real  
76 and imaginary parts of a complex number at each voxel.
- 77 • Considering the original intensity to be a complex number with zero imaginary part, add the real and  
78 imaginary components obtained above and take the magnitude of the resulting complex signal.

79 For example, Sled et al. (1998) used this approach to add noise in simulated MRIs that were used for  
80 the validation of intensity bias correction scheme they presented. Using the same approach, Camara et al.  
81 (2008) added noise to the simulated ground truth images with atrophy.

82 In addition to the Rician noise described above, other noise and artifacts are also present in MRIs  
83 (Simmons et al., 1994). Some of the artifact sources that have been shown to affect the measurements of  
84 atrophy estimation algorithms (Camara-Rey et al., 2006; Sharma et al., 2010; Pieperhoff et al., 2008) are:

- 85 • Bias field inhomogeneity arising due to poor radio frequency (RF) coil uniformity.
- 86 • Geometrical distortions that are present due to the errors in gradient field strength and non-linearity of  
87 gradient fields in the MR scanner (Langlois et al., 1999).
- 88 • Interpolation of intensities during various pre-processing steps of TBM based analysis framework (e.g.,  
89 resampling of the images into a common template space).

90 Many other acquisition artifacts may not be simulated because we do not have faithful models. Inability to  
91 produce realistic intensity variation and noise in simulated longitudinal images is one of the key limitations  
92 in the state-of-the-art atrophy simulators, including our previous work (Khanal et al., 2016b). In this work,  
93 we propose a simple but elegant solution to remove the limitation of previous atrophy simulators. First, our  
94 biophysical model of brain deformation (Khanal et al., 2016b) is used to obtain a dense deformation field  
95 with specified volume changes. Then, to obtain realistic intensity variations, intensities in the simulated  
96 images are resampled from baseline repeat scans of the same patient. Although the method is very simple  
97 and straightforward, this allows simulating longitudinal images with variation in intensity and noise taken  
98 from real scans themselves without explicitly specifying any noise or artifact models. To the best of our  
99 knowledge, this idea was not presented before in the literature. When the repeat scans are not available,  
100 we use an approach introduced by Prakosa et al. (2013) where the authors simulate visually realistic time  
101 series of cardiac images. Intensity variation in the simulated images of a patient is obtained by resampling  
102 the intensities from the repeat scans if available, otherwise from the real images of the same patient taken  
103 at different times.

104 Figure 1 shows a diagram of the complete framework. To implement this framework, we have developed  
105 an open-source atrophy simulator software called *Simul@tropy*<sup>1</sup>. To our knowledge, *Simul@tropy*  
106 is the first atrophy simulator to be made open-source. *Simul@tropy* uses the biophysical model  
107 presented in Khanal et al. (2016b) but introduces a new numerical scheme to compute divergence, which  
108 removes the numerical inconsistency presented in the previous work. This is further explained in detail in  
109 Section 4.2.

---

<sup>1</sup> Available at <https://inria-asclepios.github.io/simul-atrophy/>

110 Section 2 explains all the blocks of the framework shown in Figure 1. Starting from a small set of real  
 111 scans, we show how longitudinal images with different atrophy patterns and realistic intensity variations  
 112 can be simulated. Section 3 shows some simulation results using `Simul@trophy`, and also illustrates  
 113 some potential applications of the simulator. In Section 4, we present some example simulations to illustrate  
 114 some of the important points to consider when using `Simul@trophy` for different applications, such as  
 115 evaluation of atrophy estimation algorithms, validation of data-driven disease progression models, training  
 116 of brain morphometry algorithms based on machine learning etc.

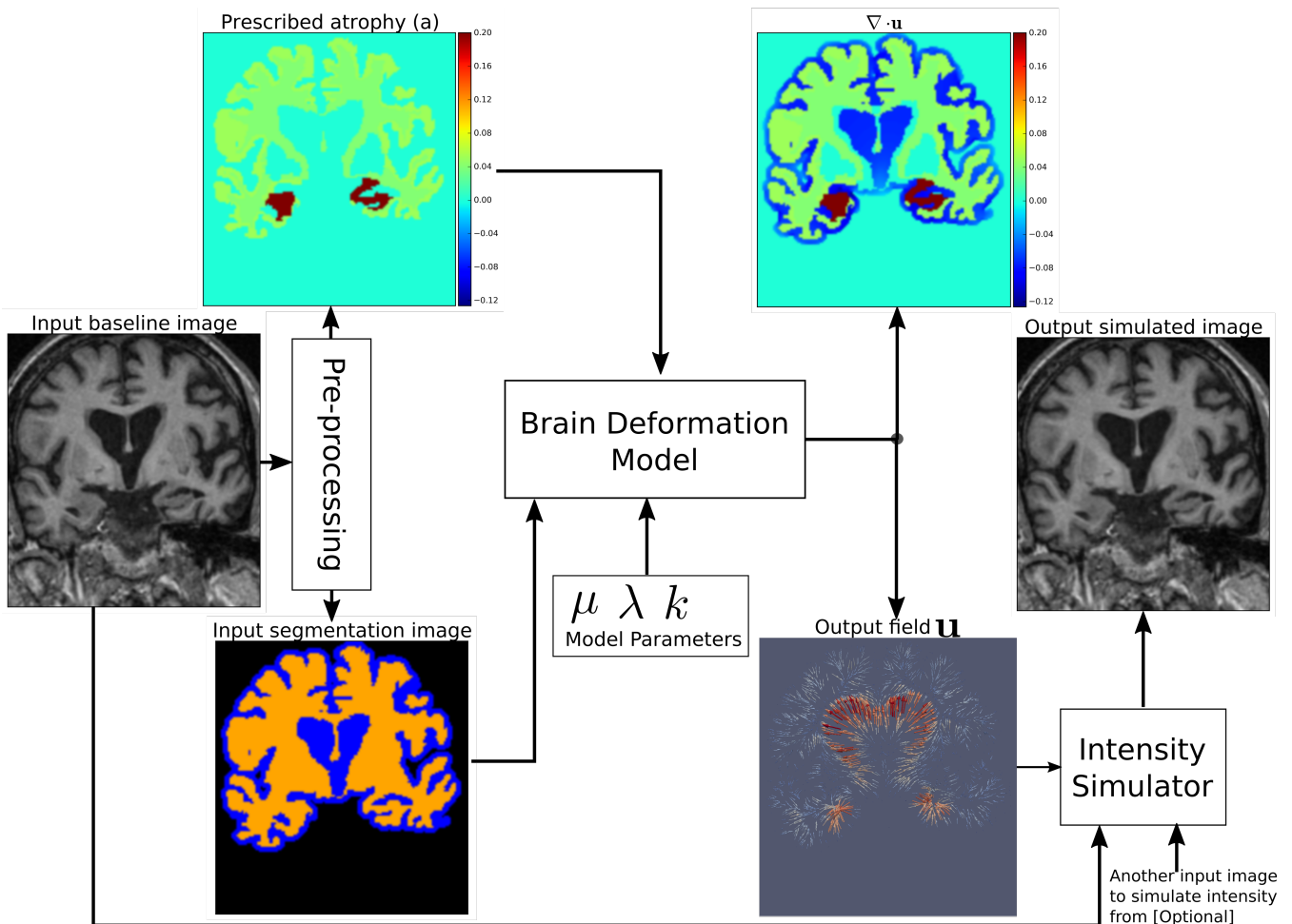


**Figure 1.** Pipeline to simulate synthetic images using `Simul@trophy`. Starting from a real baseline image of a subject, synthetic images with known volume changes can be generated. These synthetic images can follow intensity characteristics of either the input baseline or other images of the same subject. Pre-processing is required to generate an atrophy map and a segmentation image, which are fed as inputs to the brain deformation model. For a given set of parameters, the model computes a velocity field whose divergence is equal to the prescribed atrophy map at each voxel of the regions selected by using the segmentation image. Intensity simulator uses the output field to produce synthetic image whose intensity is resampled either from the input real baseline or from any other image as desired.

## 2 SIMULATING REALISTIC LONGITUDINAL IMAGES WITH ATROPHY/GROWTH

117 We use the biophysical model presented in Khanal et al. (2014, 2016b) to generate dense deformation field  
 118 with specified complex patterns of volume changes. This deformation field is then used to generate realistic

119 synthetic longitudinal images with intensity variation, noise and artifacts, just like in real longitudinal  
120 images. The major components of the simulation framework, as seen in Figure 1, are: i) Pre-processing ii)  
121 Brain deformation model iii) Realistic intensity simulator.

## 122 2.1 Pre-processing to generate a segmentation image and atrophy maps

123 A pre-processing step takes a real scan of a patient as an input baseline image, and generates the required  
124 inputs of the brain deformation model: a segmentation image and a specified atrophy map.

### 125 2.1.1 Segmentation image

126 There are three labels in the segmentation image used by `Simul@tropy` (Figure 1):

- 127 • `Label0`: regions where no deformation should be prescribed,
- 128 • `Label1`: regions where the deformation model is allowed to adapt volume changes as required,
- 129 • `Label2`: regions where certain volume changes are prescribed (the values of volume changes are  
130 provided with an input atrophy map).

131 Pre-processing usually starts with a brain extraction that excludes the skull and outside regions (also  
132 called skull stripping). Skull stripping is followed by a segmentation such that each voxel of the input  
133 image could be assigned to one of the three labels. For example, a typical pre-processing step that includes  
134 a segmentation of brain parenchyma and CSF would produce a segmentation image with the following  
135 labels:

- 136 • `Label0`: Skull and outside regions of the input image
- 137 • `Label1`: CSF regions
- 138 • `Label2`: Gray and white matter regions

### 139 2.1.2 Atrophy map

140 An atrophy map is a scalar image with desired values of volume changes in `Label1` regions of the  
141 segmentation image, and zeros in all the other regions. It is defined at each voxel as follows:

$$a = \frac{V_0 - V_1}{V_0},$$

142 where  $V_0$  and  $V_1$  are the volumes of the material lying in a voxel at time  $t_0$  and  $t_1$  respectively. Thus,  
143 regions with volume loss have positive values of  $a$  while the regions with volume expansion have negative  
144 values of  $a$ . An example atrophy map is shown in Figure 1. In this work, we illustrate example simulations  
145 where two kinds of pre-processing steps were used to generate the atrophy maps:

#### 146 Segmentation based atrophy map

147 The user can set uniform values of atrophy in regions of interests (ROIs) of the brain. In this case, one  
148 must first perform a segmentation of all ROIs in which a non-zero value of atrophy is desired. Then, it  
149 is straightforward to create a scalar image having intensity values taken from a table, which contains the  
150 labels of ROIs and the corresponding desired atrophy values.

#### 151 Registration based atrophy map

152 The results of longitudinal non-rigid registration can be used to estimate local volume changes, for instance  
153 by computing Jacobian determinants of the displacement fields or by computing the divergence of the

154 stationary velocity fields obtained from the registration. These local volume changes obtained from the  
 155 registration based methods are usually smoothly varying in space and can be used to prescribe either:

- 156 • smoothly varying atrophy maps,
- 157 • or atrophy maps uniform in ROIs obtained by averaging, in each ROIs, the atrophy obtained above.

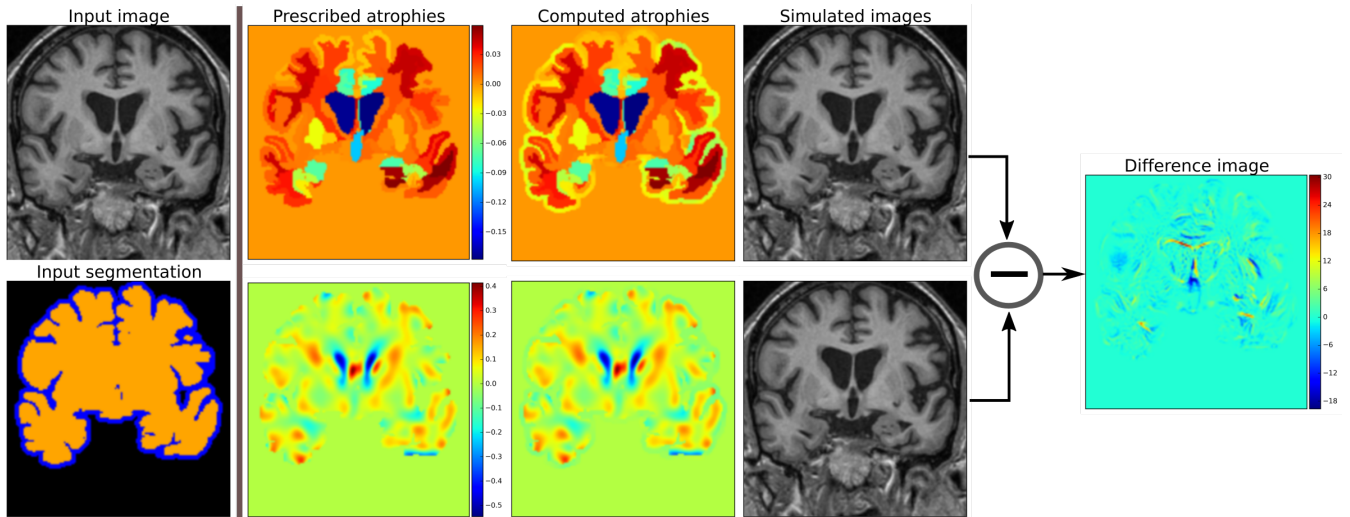


**Figure 2.** Examples of two different kinds of atrophy maps. The first row prescribes an atrophy map that is uniform in different regions of the brain, while the second row prescribes a smoothly varying atrophy. Both of these atrophy maps have same average values in each ROIs. The example also shows that we can prescribe volume changes in ventricles, if desired, by adapting the input segmentation map accordingly. The simulated images, as shown, are different although they have same mean regional atrophy values. The prescribed atrophy maps and the corresponding computed atrophy maps have different values of atrophy in the regions with sulcal CSF because it is part of `Label1` (blue color in the segmentation map) where the volume is allowed to freely change.

158 Figure 2 shows two such atrophy maps with very different patterns, but having the same average regional  
 159 volume changes.

## 160 2.2 A biophysical model of brain deformation with prescribed volume changes

161 `Simul@trophy` uses the biomechanics based model of brain deformation detailed in Khanal et al.  
 162 (2016b). The model abstracts the phenomenon that evolves during several months or years in the brain at a  
 163 macroscopic scale. It is based on the assumption that atrophy creates an internal stress which results in the  
 164 deformation minimizing a strain energy. In other words, the brain parenchyma deforms with the prescribed  
 165 atrophy by minimizing the strain energy. The strain energy corresponding to the prescribed atrophy at each  
 166 time step is completely released when starting the next time step, which leads to a creep flow model.

167 For a given segmentation image, the model yields a deformation field with the prescribed atrophy at each  
 168 voxel of `Label2` regions (e.g. brain parenchyma). `Label1` regions (e.g. the CSF) will correspondingly  
 169 adapt its volume to globally compensate for the prescribed volume changes in the `Label2` regions. For  
 170 a single time-step, the displacement field  $\mathbf{u}$  is obtained by solving the system of Eqs 1, where Dirichlet  
 171 boundary conditions of zero deformation are prescribed in `Label0` regions.

$$\left. \begin{array}{l} \text{Regions with: Label10} \\ \mathbf{u} = 0 \\ \text{Dirichlet boundary conditions} \end{array} \right\} \quad \left. \begin{array}{l} \text{Label11} \\ \mu\Delta\mathbf{u} - \nabla p=0 \\ \nabla \cdot \mathbf{u} + kp=0 \end{array} \right\} \quad \left. \begin{array}{l} \text{Label12} \\ \mu\Delta\mathbf{u} - \nabla p=(\mu + \lambda)\nabla a \\ \nabla \cdot \mathbf{u} = -a \end{array} \right\} \quad (1)$$

172 The system of Eqs. 1 shows that the incompressibility constraint is relaxed in Label11 regions, while it  
173 is strictly satisfied in Label12 regions.

174 The prescribed atrophy map  $a$  in the constraint  $\nabla \cdot \mathbf{u} = -a$  is the amount of atrophy in a small time step  
175  $\Delta t$  such that the displacement field  $\mathbf{u}$  and its gradient are small enough to make the following approximation:  
176  $\nabla \cdot \mathbf{u} = -a \approx J - 1$ , where  $J$  is the Jacobian determinant (Khanal et al., 2016b). Jacobian determinant  
177 measures the relative volume of a warped voxel,  $V_1/V_0$ .

178 The impact of the choice of different values for the model parameters  $\mu$ ,  $\lambda$  and  $k$  are detailed in Khanal  
179 et al. (2016b). For the same prescribed volume changes, we can obtain different deformation fields by  
180 varying these model parameters. In this work, we focus on generating ground truth images with known  
181 volume changes and not necessarily generating the exact evolution of the AD patients. Hence, we set the  
182 model parameters as follows unless specified otherwise:  $\mu = 1$  kPa,  $\lambda = 0$  kPa,  $k = 1$  kPa<sup>-1</sup>.

183 Once the field  $\mathbf{u}$  with the prescribed volume changes is obtained from the model as described above by  
184 using an input baseline image  $I_b$ , we can simulate a synthetic follow-up image  $I_s$  as follows:

- 185 • Let  $\mathbf{y} = \Phi_{\text{sim}}(\mathbf{x}) = \mathbf{u} + \mathbf{x}$  describe a mapping of a point  $\mathbf{x}$  in physical space to another point  $\mathbf{y}$  by  
186 applying the transformation corresponding to the dense deformation field  $\Phi_{\text{sim}}$ , or the displacement  
187 field  $\mathbf{u}$ .
- 188 • Let  $\Phi_{\text{sim}} \star I_b$  describe an action of the diffeomorphism  $\Phi_{\text{sim}}$  on the image  $I_b$ . Thus, the new synthetic  
189 image  $I_s$ , obtained by warping  $I_b$  with the deformation field  $\Phi_{\text{sim}}$  is given by:

$$I_s = \Phi_{\text{sim}} \star I_b = I_b \circ \Phi_{\text{sim}}^{-1}.$$

190 Figure 2 shows two simulated images from the same input baseline image but with two different atrophy  
191 patterns.

### 192 2.3 Adding realistic intensity variation to synthetic longitudinal MRIs

193 In realistic scenarios, longitudinal MRIs are taken at multiple scan sessions often with slightly different  
194 acquisition parameters or even with different scanners. For generating more realistic synthetic longitudinal  
195 MRIs, variations in intensity and noise present in real longitudinal MRIs must also be simulated. If multiple  
196 repeat scans of a subject are available, we can use them to simulate such variations in synthetic longitudinal  
197 sequences. Assuming that all the available scans of the subject are already aligned using affine registration,  
198 this section explains the proposed method of adding realistic variations in the intensity characteristics.

199 Starting from an input baseline image  $I_{b_0}$  of a subject, the previous sections explained how we can obtain  
200 a deformation field  $\Phi_{\text{sim}}$  from the brain deformation model, and use it to simulate a follow-up image

$$I_{s_0} = \Phi_{\text{sim}} \star I_{b_0}.$$



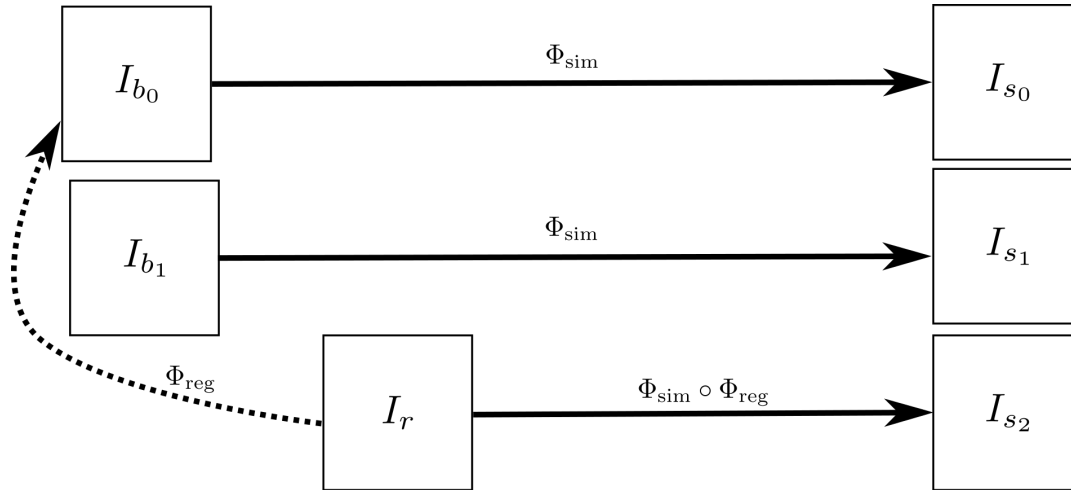


**Figure 3.**  $I_{b_0}$  and  $I_{b_1}$  are the repeat scans of a subject taken within a short period of time during which there is no morphological changes in the brain of the subject.  $I_r$  is taken at a later time when the brain could have undergone some morphological changes. The deformation field  $\Phi_{reg}$  is obtained by registering  $I_r$  to  $I_{b_0}$ , while  $\Phi_{sim}$  is obtained from the brain deformation model using  $I_{b_0}$  as the input image. The three simulated images  $I_{s_0}$ ,  $I_{s_1}$  and  $I_{s_2}$  are all same time-point images but have different intensities that come from  $I_{b_0}$ ,  $I_{b_1}$  and  $I_r$  respectively.

201  $I_{s_0}$  has the same intensity characteristics as  $I_{b_0}$ , and the intensity noise in  $I_{s_0}$  is strongly correlated to the  
 202 noise present in  $I_{b_0}$ .

203 If  $I_{b_1}$  is another scan of the same subject taken on the same day, we can obtain a new simulated image by  
 204 resampling the intensity from  $I_{b_1}$ , but still using the same  $\Phi_{sim}$ :

$$I_{s_1} = \Phi_{sim} \star I_{b_1}$$

205 The realistic variation of intensity and artifacts present between the two real scans  $I_{b_0}$  and  $I_{b_1}$  are now also  
 206 present between the real baseline image  $I_{b_0}$  and the simulated follow-up image  $I_{s_1}$ .

207 The above approach assumes that the brain has not undergone any morphological changes between the  
 208 scan sessions of the two real images. If the scan time-points of the two images are too far apart to have this  
 209 assumption valid, we can no longer directly apply  $\Phi_{sim}$  to the second image. Let  $I_r$  be another real scan of  
 210 the patient taken at a time later than that of the baseline image  $I_{b_0}$ . There might be some morphological  
 211 changes (e.g. atrophy) in  $I_r$  compared to  $I_{b_0}$ .

212 To simulate a new synthetic image with the same atrophy as that of  $I_{s_0}$  but with the intensity resampled  
 213 from  $I_r$ , we must first perform a non-rigid registration between  $I_r$  and  $I_{b_0}$ . If  $\Phi_{reg}$  is the deformation field  
 214 obtained from the non-rigid registration between  $I_r$  and  $I_{b_0}$ , it can be used to get an image  $\Phi_{reg} \star I_r$  which  
 215 is aligned to  $I_{b_0}$ . In the ideal case,  $\Phi_{reg} \star I_r$  and  $I_{b_0}$  are perfectly aligned with the only differences lying in  
 216 the intensity characteristics and the noise.

217 We can now compose the deformation fields  $\Phi_{sim}$  and  $\Phi_{reg}$  to generate a new synthetic image as follows:

$$I_{s_2} = (\Phi_{sim} \circ \Phi_{reg}) \star I_r.$$

218  $I_{s_2}$  has the same atrophy as that of  $I_{s_0}$  but with the intensity characteristics of  $I_r$ . Figure 3 illustrates how  
 219 we obtain  $I_{s_0}$ ,  $I_{s_1}$  and  $I_{s_2}$ . These three simulated images have the volume changes as encoded by  $\Phi_{sim}$ , but  
 220 have intensity characteristics coming from three different real images of the same patient.

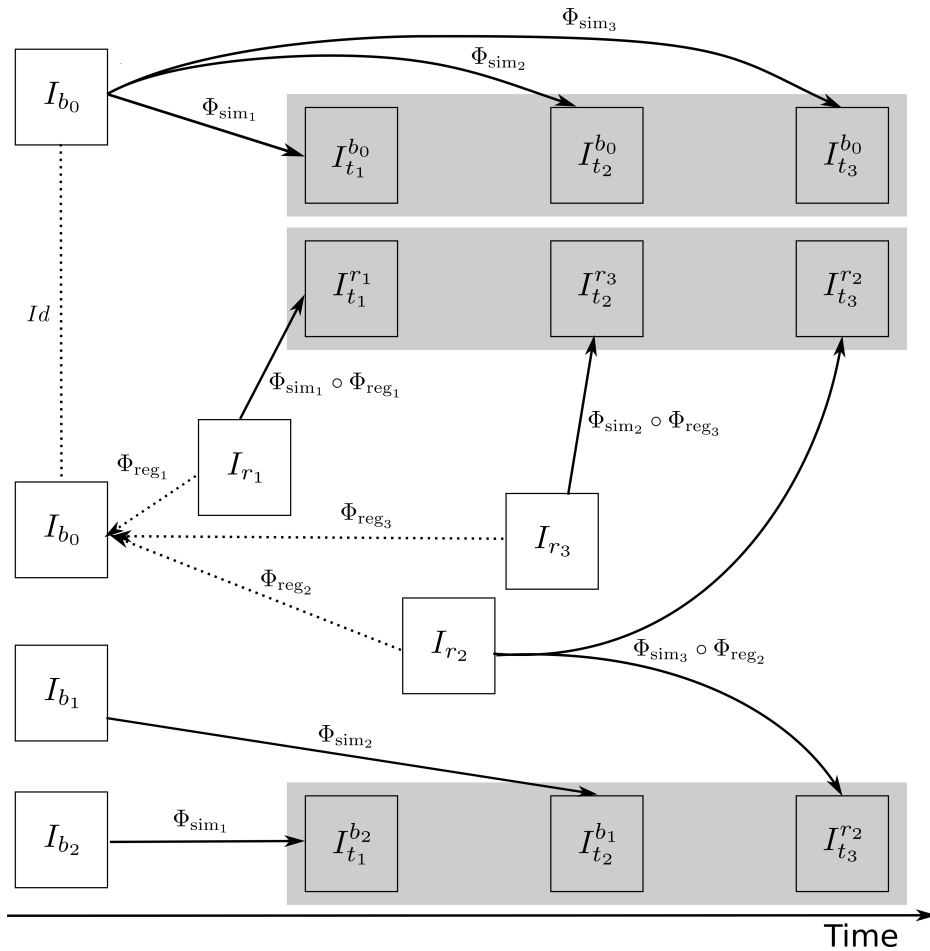


**Figure 4.** A general approach to simulate ground truth synthetic longitudinal images with realistic intensity variations; simulated images are shown within the shaded regions. The deformation fields with a prescribed atrophy for three time-points ( $\Phi_{sim_1}$ ,  $\Phi_{sim_2}$ , and  $\Phi_{sim_3}$ ) are obtained from the biophysical model using  $I_{b_0}$  as the input baseline image. Several different sets of longitudinal images can then be simulated by resampling intensities from different combinations of available real images. The topmost shaded region shows a longitudinal sequence with no realistic intensity variations where the synthetic images are all resampled from  $I_{b_0}$ . The remaining two shaded regions have longitudinal sequences with realistic intensity variations where the simulated images are resampled from other available images of the same subject. In the ideal case, the three sets of longitudinal sequences have exactly the same morphological changes but with different variations in intensity characteristics.

221 Figure 4 illustrates how the approach described in this section can be used to generate multiple sets  
 222 of longitudinal simulated sequences having identical morphological evolution but different variations of  
 223 intensities. The three shaded regions in Figure 4 are the sets of longitudinal sequences with identical  
 224 volume changes but with different variations of intensities.

### 3 SIMULATION EXAMPLES WITH SIMUL@TROPHY

225 This section presents simulation examples of synthetic longitudinal MRIs with prescribed atrophy patterns  
 226 and realistic intensity variations<sup>2</sup>. The real input MRIs used for the simulations presented in this section  
 227 come from the database made available by Hadj-Hamou et al. (2016). The images had already undergone the  
 228 `Pre-Processing and Position Correction` steps of the Longitudinal Log-Demons Framework  
 229 (LLDF) detailed in Hadj-Hamou et al. (2016). Starting from the publicly available OASIS dataset (Marcus  
 230 et al., 2010), the images in the database had undergone intensity inhomogeneity correction using `ANTs -`  
 231 `N4BiasFieldCorrection` (Avants et al., 2011), and had been transported to a common space using  
 232 affine registration with `FSL - FLIRT` (Jenkinson and Smith, 2001).

233 Since all the simulated images must undergo interpolation of intensities, numerical scheme used in  
 234 the interpolation will have an impact on the intensity characteristics of the simulated images. In all the  
 235 simulation examples that follows, intensities were resampled using B-spline interpolation of order 3.

236 Figure 5 shows a simulation example where uniform atrophy patterns are prescribed in the hippocampi,  
 237 the gray matter (GM), and the white matter (WM) regions. The ventricles and sulcal CSF regions are  
 238 allowed to expand as required to compensate for the volume loss in the brain parenchyma. The figure  
 239 shows two simulated images whose intensities are resampled from two different images: i) the input  
 240 baseline image  $I_b$  ii) another follow-up image of the same subject,  $I_r$ . The figure also shows intensity  
 241 histograms of these two simulated images for a selected ROI. The selected ROI is a 2D WM region where  
 242 the simulated images do not have a distinct morphological changes from  $I_b$ . Thus, the differences in the  
 243 intensity histograms of  $I_b$  and the simulated images for this ROI is mostly due to the variation in intensity  
 244 characteristics of the different images. We can see from the figure that the intensity characteristics of the  
 245 simulated image resampled from  $I_b$  closely matches the intensity characteristics of  $I_b$ . And resampling the  
 246 intensity from a different image  $I_r$  of the same subject allows simulating realistic variation of intensities.

247 To simulate multiple time-point images, the following approach can be used:

- 248 • Get  $\mathbf{u}_0$  by solving the system of Eqs. (1) using the initial atrophy map  $a_0$  and the initial segmentation  
 249 image  $L_0$  as input.
- 250 • For each time step  $t = 1$  to  $n$ :
  - 251 • Warp  $a_{t-1}$  and  $L_0$  using  $\mathbf{u}_{t-1} \circ \mathbf{u}_{t-2} \dots \circ \mathbf{u}_0$  to get  $a_t$  and  $L_t$  respectively.
  - 252 • Solve for  $\mathbf{u}_t$  using  $a_t$  and  $L_t$  as input.

253 Once all the deformation fields  $\Phi_{s_i}$  corresponding to  $\mathbf{u}_i$  for  $i = 0, 1, \dots, n$  are obtained, these deformation  
 254 fields can be used as shown in Figure 4 to simulate different sequences of longitudinal images. As time step  
 255 gets larger, the segmentation map is warped with an increasingly bigger displacement field using nearest  
 256 neighbor interpolation, which could result in numerical instabilities. As the atrophy map is also warped at  
 257 each time step, the global atrophy rate prescribed in the beginning is not necessarily preserved during the  
 258 intermediate time-steps.

259 In Figure 6, a simulation example of two longitudinal sequences each having three new time-point images  
 260 is shown. Both sequences were simulated by prescribing a smoothly varying atrophy pattern. The smoothly  
 261 varying atrophy pattern prescribed in this example is more complex than the simple pattern used in the  
 262 previous example. In brain parenchyma regions, it is the negative of the divergence of a stationary velocity  
 263 field obtained by performing LCC log-Demons registration (Lorenzi et al., 2013) of the input baseline

<sup>2</sup> The simulation results are made available at <http://neurovault.org/collections/AUKWWYBC/> (Gorgolewski et al., 2015).

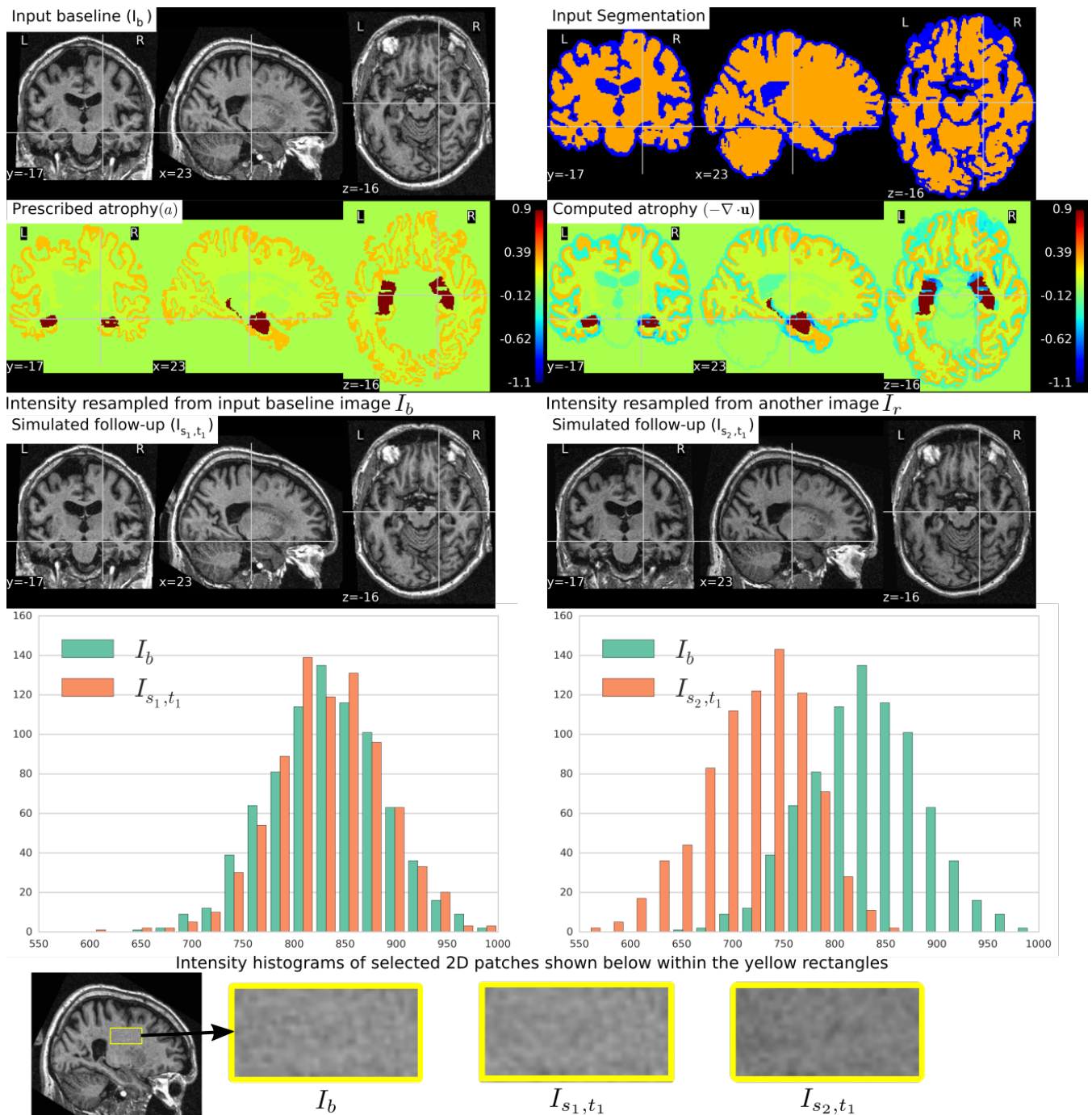


**Figure 5.** Two simulated images are shown on the third row where the image on the left is resampled from the input baseline image  $I_b$ , and the image on the right is resampled from another image  $I_r$  of the same subject. Both  $I_b$  and  $I_r$  had already been corrected for the bias field intensity inhomogeneity. The intensity histograms shown are of a selected ROI (shown on the last row) where there is no significant morphological changes between the images. From the histograms we can see that the simulated image  $I_{s_2, t_1}$  has a different intensity characteristics than  $I_b$ , while the simulated image  $I_{s_1, t_1}$  has intensity characteristics that closely matches to that of  $I_b$ .

264 image with a follow-up image of the same subject. The first sequence consists of all the images whose  
 265 intensities are resampled from the same input baseline image  $I_b$ , while the second sequence consists of the  
 266 images whose intensities are resampled from different real MRIs of the same subject. Thus, as shown in

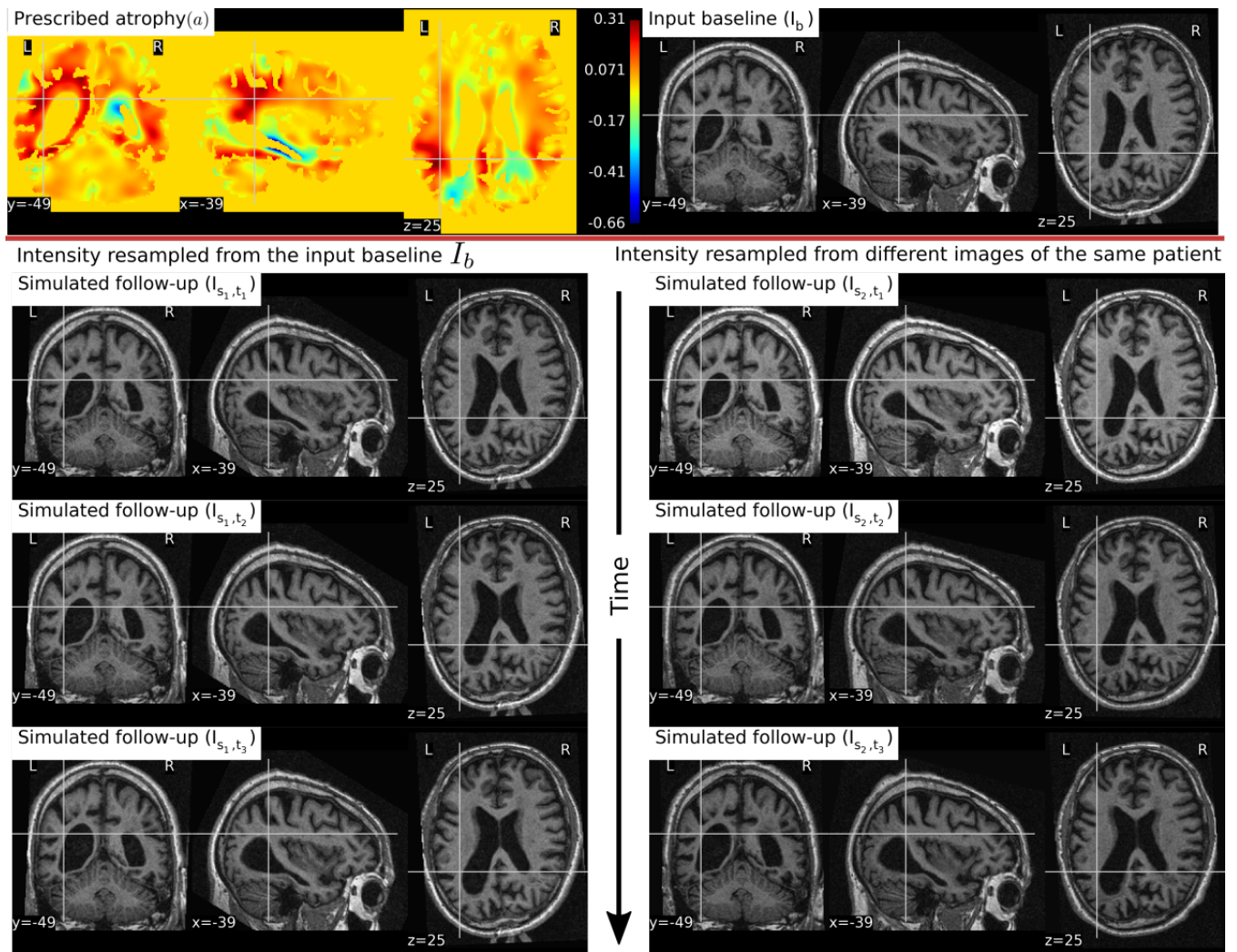


**Figure 6.** Two sets of synthetic longitudinal images are shown which are simulated by prescribing a smoothly varying atrophy pattern. The first row shows the input prescribed atrophy and the input baseline image  $I_b$  of a subject, while the remaining rows show the two sequences. The sequence shown on the left have simulated images that are all resampled from  $I_b$ . On the right, each simulated image is resampled from real MRIs of the same subject but taken at different times (at 0.68, 1.77 and 3.3 years after the baseline scan respectively). As shown by the intensity histograms of Figure 7, the longitudinal synthetic images on the right have more realistic intensity variations than the one left.

267 Figure 7, the first sequence does not have the realistic variation of intensities while the second sequence  
 268 has the realistic variation of intensities. With this example, we also illustrated that we can generate multiple  
 269 sequences of longitudinal images with same atrophy patterns but different variations of intensities.

270 Figure 8 shows a simulation example where we prescribe growth instead of atrophy in the brain tissue.  
 271 The prescribed atrophy in this case is the negative of the atrophy map prescribed in Figure 6. From the  
 272 segmentation image shown in Figure 8, we can see that the ventricles were allowed to adapt the volume  
 273 changes as required to compensate for the volume changes in the brain parenchyma. From the three  
 274 simulated time-points, we can see that these ventricles are shrinking and the brain parenchyma regions are  
 275 expanding. The example shows that `Simul@tropy` can be used to simulate images of not only future  
 276 time-points, but also the past time-point images.

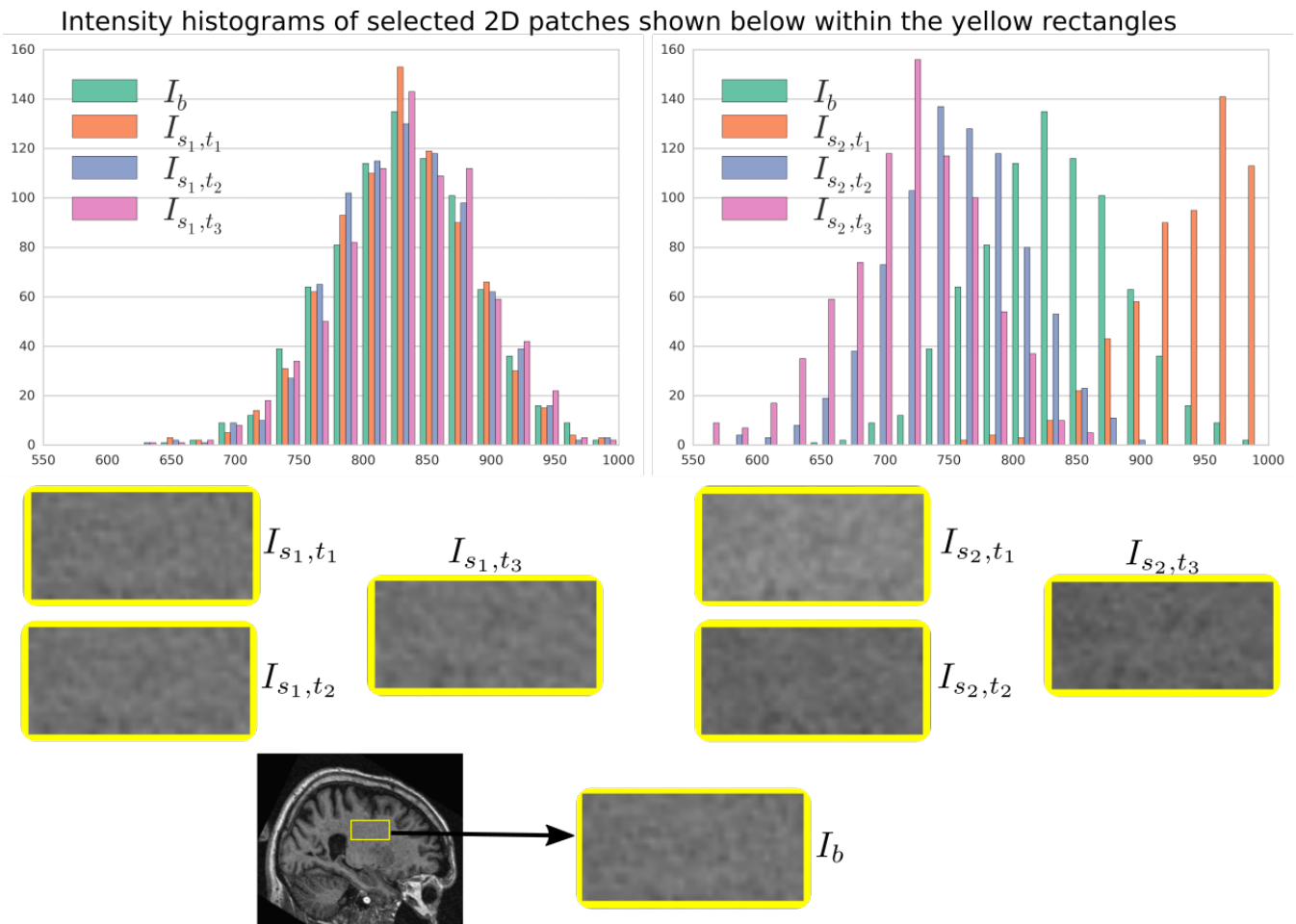


**Figure 7.** Intensity histograms of selected patches of the images simulated in Figure 6. When the simulated images are resampled from the same input baseline image  $I_b$ , as expected, the histograms of the simulated images closely match with each other. However, when simulated images are resampled from other different images of the same patients, the histograms of these simulated images do not match closely. The longitudinal sequence of simulated images  $I_{s_2,t_1}$ ,  $I_{s_2,t_2}$  and  $I_{s_2,t_3}$  has realistic variation in intensities as observed in the real sequences.

277 In Figure 9, we show an example where synthetic sequence of images is simulated by starting from a  
 278 baseline image of a healthy subject. However, the prescribed atrophy is derived from an atrophy estimated  
 279 from the AD patient used in Figure 6. The input baseline images of both the AD patient and the healthy  
 280 subject were segmented using FreeSurfer (Fischl et al., 2002). In all the segmented regions including the  
 281 white matter parcellations of the AD patient, the average values of the smoothly varying atrophy map  
 282 were computed. These regional average values of the atrophy computed from the AD patient were then  
 283 transported to the corresponding regions of the healthy subject. Thus, in Figure 9, we can see that the  
 284 prescribed atrophy is region-wise uniform instead of smoothly varying. For comparison, the figure also  
 285 shows three real time-point images of the healthy subject along with the three simulated time-point images  
 286 with atrophy derived from the AD patient.

#### 4 SIMUL@TROPHY: CHOICES AVAILABLE AND PRACTICAL CONSIDERATIONS

287 Simul@tropy is available as an open-source repository under git version control. Researchers can use  
 288 it according to their needs, improve the presented model, and/or add new models of brain atrophy. It is

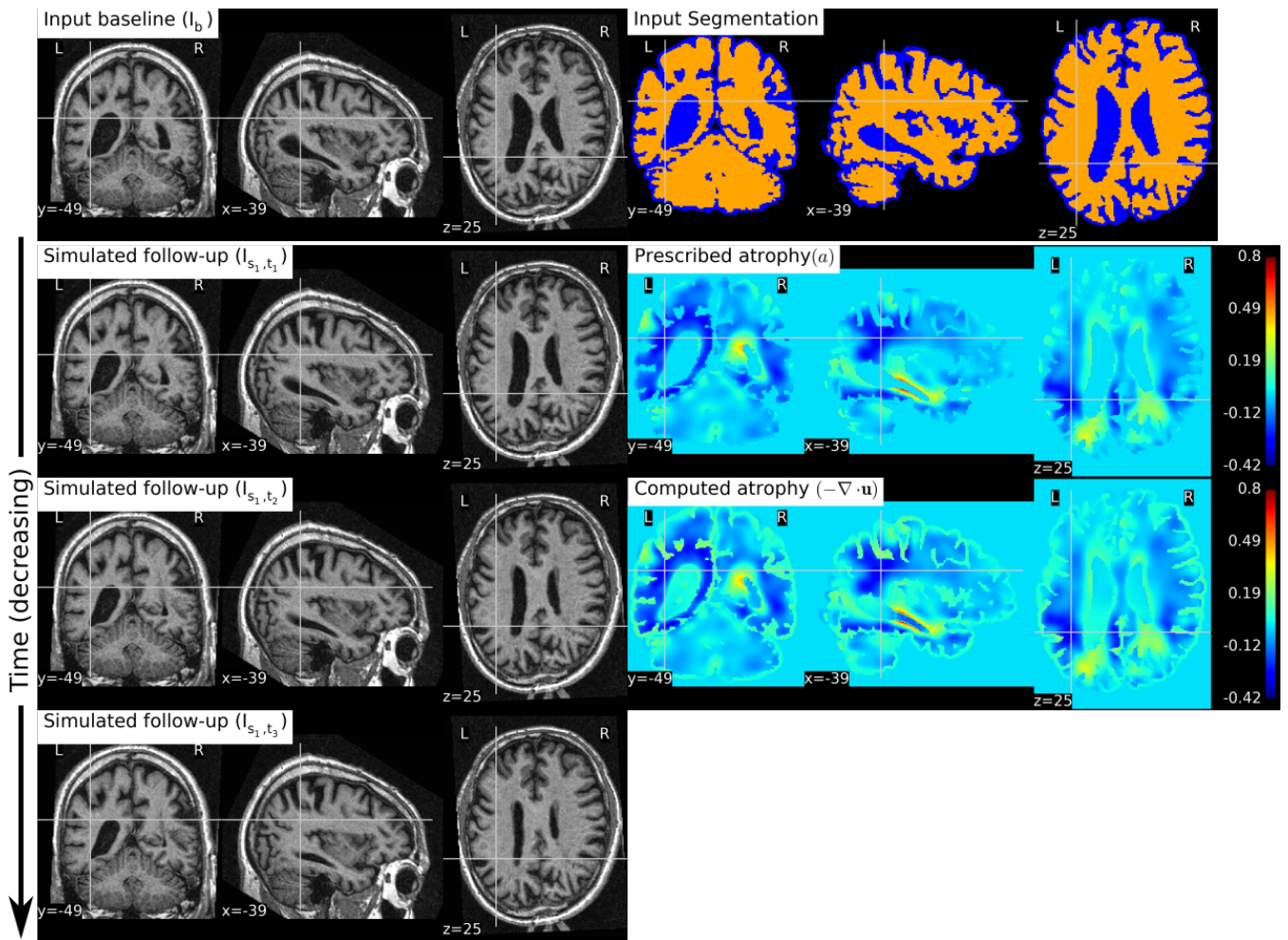


**Figure 8.** The figure shows an example of simulating a longitudinal sequence with backward time-points. The input baseline image  $I_b$  is the same one as used in Figure 6, and the prescribed atrophy map is the negative of the map used in Figure 6. In the figure, we can see the shrinkage of the ventricles and the growth of the brain parenchyma.

289 based on two core components: i) The Insight ToolKit (ITK) and ii) PETSc Balay et al. (2013). All the  
 290 input and output images of the brain deformation model shown in Figure 1 can be in any format that ITK  
 291 supports. ITK has strongly promoted reproducible science in the medical imaging domain, and has been  
 292 widely used in computational science applied to medical imaging (McCormick et al., 2014; Avants et al.,  
 293 2015). Similarly, implementation of the model solver is based on open-source PETSc, a library based on C  
 294 programming language. It has also been very widely used in a very diverse set of applications that also  
 295 include the medical field. It is a very powerful library that supports wide range of iterative solvers and  
 296 preconditioners for large systems of equations. The solvers implemented in PETSc can scale very well to  
 297 large distributive computer systems.

298 `Simul@trophy` runs from command lines where the required inputs and optional choices are provided  
 299 via command line arguments. The available command lines are detailed in Appendix 7. In this section, we  
 300 illustrate some examples of how certain choices made during the simulation affect output results.

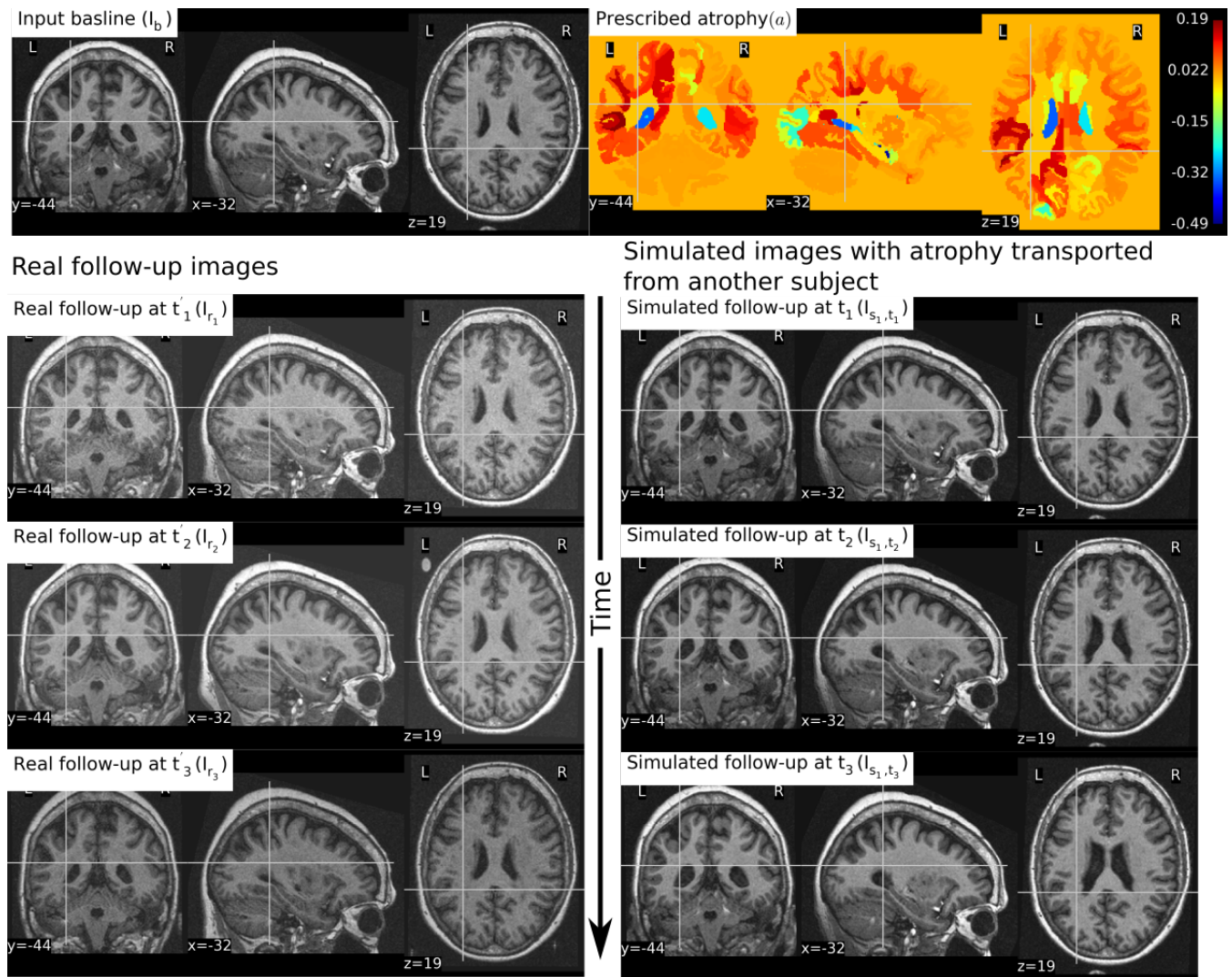


**Figure 9.** The figure shows an example of simulating follow-up images of a normal subject with baseline image  $I_b$ , where the prescribed atrophy pattern is adapted from an AD patient. The prescribed atrophy is adapted from the atrophy estimated for the AD patient shown in Figure 6. Average values of the smoothly varying prescribed atrophy shown in Figure 6 is computed in all the ROIs. The ROIs are obtained from the FreeSurfer segmentation including all the white matter parcellations (Fischl et al., 2002). The simulated images on the right have bigger shrinkage of the brain parenchyma and bigger expansion of the ventricles than the real images on the left.

301 **4.1 Impact of registration on simulated images**

302 In Section 2.3, we explained that starting from an input baseline image of a subject,  $I_b$ , we can generate  
 303 two synthetic images:

$$I_{s1} = \Phi_{sim} \star I_f \quad \text{and} \quad I_{s2} = (\Phi_{sim} \circ \Phi_{reg}) \star I_f$$

304 where  $\Phi_{sim}$  is the deformation field obtained from the brain deformation model using  $I_b$  as the input  
 305 baseline image, and  $\Phi_{reg}$  is the deformation field obtained from the non-rigid registration between  $I_b$  and a  
 306 real follow-up image  $I_f$ . Perfect alignment of the two images with a non-rigid registration is possible only  
 307 in the ideal case scenario. In such an ideal case, the simulated images  $I_{s1}$  and  $I_{s2}$  have identical shapes of  
 308 the brain structures with the only differences lying in the intensity characteristics. In practice, this is almost



309 never the case, and we present below an example of the impact of registration result on the simulated  
 310 images.

311 Let us use the following short notations for various images described in this section.

- 312 • RB: Real baseline image:  $I_b$
- 313 • RF: Real follow-up image:  $I_f$
- 314 • RB\_to\_RF: Real baseline aligned to real follow-up:  $\Phi_{\text{reg}}^{-1} \star I_b$
- 315 • SF\_in\_RB: Simulated follow-up image with intensity resampled from  $I_b$ :  $\Phi_s \star I_b$
- 316 • SF\_in\_RF: Simulated follow-up image with intensity resampled from  $I_f$ :  $(\Phi_s \circ \Phi_{\text{reg}}) \star I_f$

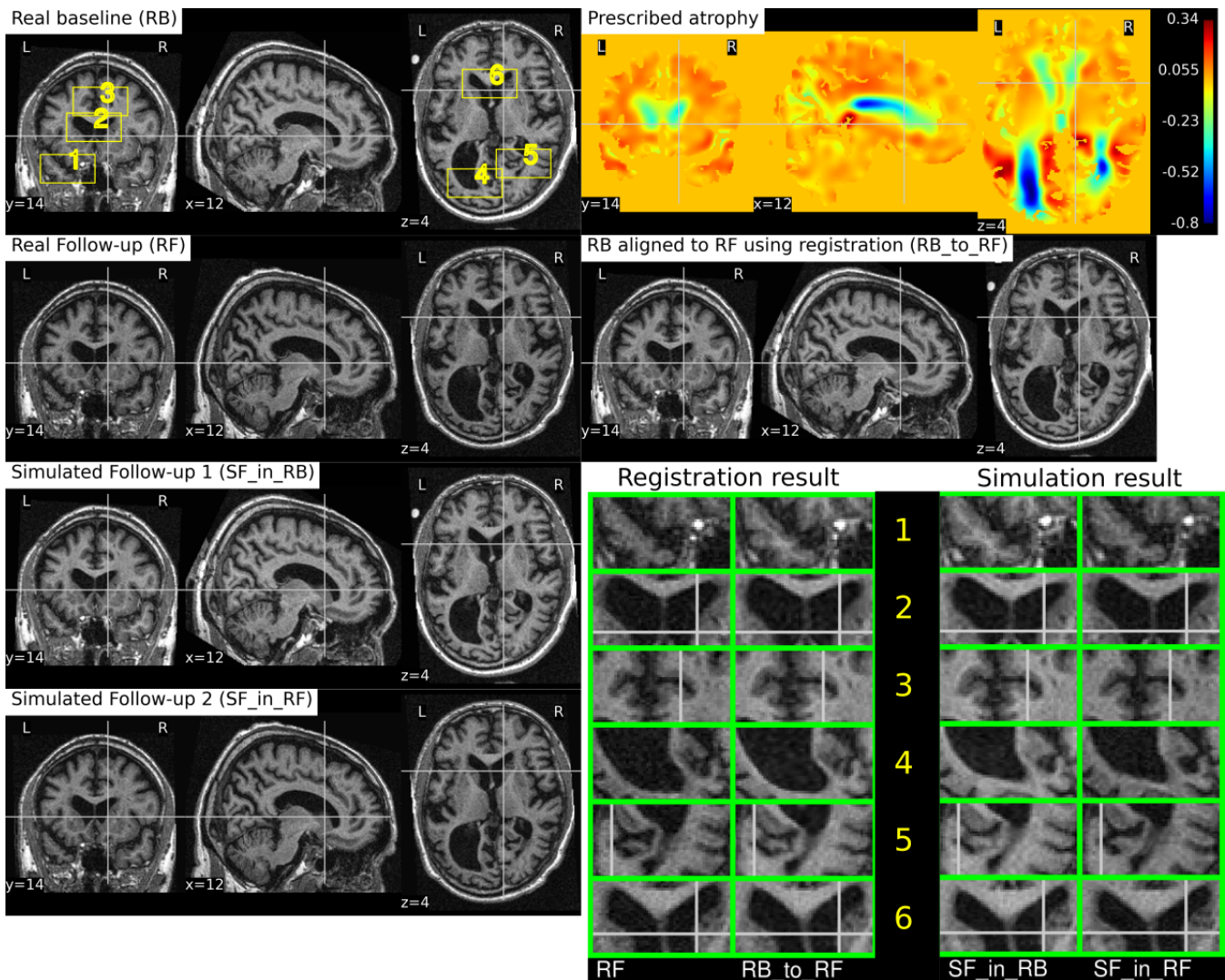


**Figure 10.** RB and RF are non-rigidly registered and the transformation obtained from the registration is used to align RB to RF which is shown in the image RB\_to\_RF. The figure also shows two simulated follow-up images SF\_in\_RB and SF\_in\_RF that are resampled from (RB) and (RF) respectively. We can see that in most regions of the brain, the two simulated images have almost identical morphological appearances. However, there are also regions such as 2 and 5, where the morphological appearances of the two simulated images are not identical. From the registration results for these regions 2 and 5 in the zoomed patches, we can see that the registration is also not accurate in those regions.

317 Figure 10 illustrates the impact of registration result  $\Phi_{\text{reg}}$  on the simulation results. The figure shows  
 318 both the registration and simulation results along with zoomed patches of RB, RB\_to\_RF, SF\_in\_RB  
 319 and SF\_in\_RF. As expected, SF\_in\_RB and SF\_in\_RF have different intensity characteristics coming  
 320 from RB and RF respectively. In the regions where registration is accurate, the two simulated images look  
 321 almost identical except for the differences in the intensity characteristics. However, in the regions where  
 322 registration is not accurate enough, SF\_in\_RB and SF\_in\_RF do not have identical shapes as expected.  
 323 Thus, for the proposed method of using deformations obtained by registration for simulation, it might be  
 324 preferable to use aggressive non-linear registrations with a much bigger weight given to similarity terms  
 325 than the regularization terms.

## 326 4.2 Discretization scheme for the divergence computation

327 In Khanal et al. (2016b), a standard staggered grid discretization was used for solving the system of Eqs.  
 328 (1). The discretization scheme is shown in Figure 11 in 2D for illustration; explanation on 2D extends  
 329 naturally to 3D. In the figure, we can see that the components of the displacement field variable  $\mathbf{u}$  lie on  
 330 cell faces and not at cell centres. However, all the input and output images for the model, including the  
 331 output displacement field image, are standard images that have their values lying in cell centres or voxels.  
 332 Our implementation of the solver internally creates the required staggered grid for the given input images.  
 333 Once  $\mathbf{u}$  is computed within the solver of system of Eqs.(1), its values at cell faces are interpolated to obtain  
 334 the values at cell centres which are then assembled to send as output displacement field image. Within the  
 335 solver, the numerical scheme used for the discretization of  $\nabla \cdot \mathbf{u} = -a$  is:

$$\frac{u_{i+1/2,j,k} - u_{i-1/2,j,k}}{h_x} + \frac{v_{i,j+1/2,k} - v_{i,j-1/2,k}}{h_y} + \frac{w_{i,j,k+1/2} - w_{i,j,k-1/2}}{h_z} = a_{i,j,k} \quad (2)$$

336 where,

$$\mathbf{u} = \begin{pmatrix} u \\ v \\ w \end{pmatrix}.$$

337 Simul@trophY then provides output displacement field image with the values of  $\mathbf{u}$  lying at cell centres  
 338 or voxels by using linear interpolation as follows:

$$\begin{pmatrix} u_{i,j,k} \\ v_{i,j,k} \\ w_{i,j,k} \end{pmatrix} = \begin{pmatrix} (u_{i+1/2,j,k} + u_{i-1/2,j,k}) / 2 \\ (v_{i,j+1/2,k} + v_{i,j-1/2,k}) / 2 \\ (w_{i,j,k+1/2} + w_{i,j,k-1/2}) / 2 \end{pmatrix} \quad (3)$$

339 To compare divergence maps of this output field with the ones obtained from tools external of  
 340 Simul@trophY, the only accessible values are the interpolated ones. ITK is widely used in registration  
 341 based brain morphometry algorithms, but the default derivative computation of ITK has the following  
 342 centred difference stencil:

$$\frac{u_{i+1,j,k} - u_{i-1,j,k}}{2 * h_x} + \frac{v_{i,j+1,k} - v_{i,j-1,k}}{2 * h_y} + \frac{w_{i,j,k+1} - w_{i,j,k-1}}{2 * h_z} = a_{i,j,k} \quad (4)$$

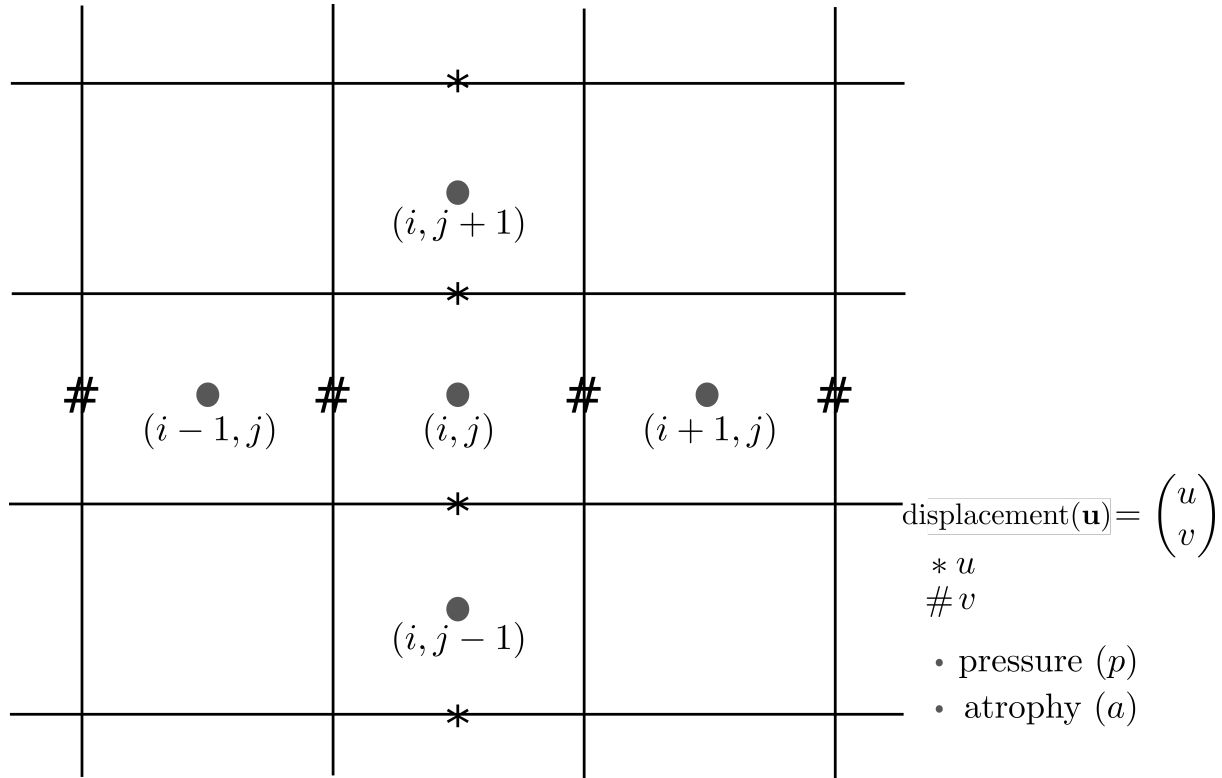


**Figure 11.** Standard staggered grid discretization scheme that is used to solve the system of Eqs. (1). Displacement variables are at faces (edges in 2D) of the cells, while pressure and atrophy values are at centres of the cells.

343 Replacing the components of  $\mathbf{u}$  at cell centres from Eq. 3, we get,

$$\frac{u_{i+3/2,j,k} + u_{i+1/2,j,k} - (u_{i-1/2,j,k} + u_{i+3/2,j,k})}{4 * h_x} + \dots = a_{i,j,k} \quad (5)$$

344 The scheme in Eq. (5) does not match the one that was used internally by `Simul@trophy` shown in  
 345 Eq. (2). This results in discrepancy if we compare input prescribed atrophy maps against the externally  
 346 computed divergence maps  $\nabla \cdot \mathbf{u}$ . Thus, in this work, we have added an implementation for the scheme  
 347 in Eq. (5) so that users can choose either of the two possible schemes of Eq. (2) and Eq. (5). The latter  
 348 scheme is consistent with the divergence computed by the default derivative computation options of ITK.  
 349 At each 3D cell, the scheme in Eq. (2) involves 6 variables of the displacement field, while the scheme in  
 350 Eq. (5) involves 12 variables. In the rest of the paper, they will be referred to as 6-point and 12-point  
 351 schemes respectively.

352 Figure 12 shows the error in specified vs. obtained atrophy when using the two different numerical  
 353 schemes. As expected, we can see that when a consistent numerical scheme is used, there is no difference  
 354 between the specified and obtained atrophy. When the schemes are not consistent, the error is larger on the  
 355 areas where the prescribed atrophy values change sharply.

356 If the simulated ground truth images using `Simul@trophy` are used for the evaluation of atrophy  
 357 estimation algorithms, one must also be careful about the measure of volume change used in addition to  
 358 the numerical scheme used. For instance, many TBM based brain morphometry algorithms use Jacobian  
 359 determinants as a measure of volume change. To compute ground truth volume changes of the simulated

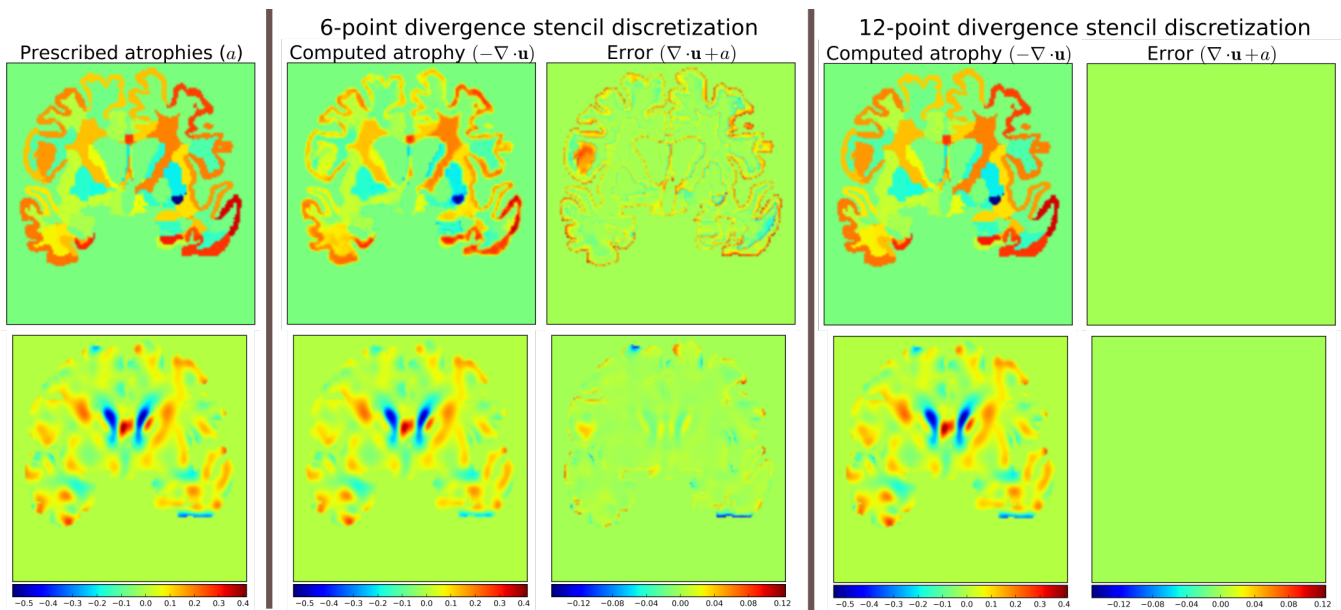


**Figure 12.** Error due to non-consistent numerical schemes in Eq. (2), and Eqs. (4 and 5).  $\nabla \cdot \mathbf{u}$  shown in the figure are computed external of `Simul@troph` by using the default ITK derivative computation scheme shown in Eq. (4). When this divergence computation is consistent with the one used in `Simul@troph`, we should obtain zero error with  $\nabla \cdot \mathbf{u} + a = 0$ . This is indeed the case, as seen on the right, when we use 12-point stencil of Eq. 5. We see non-zero errors when using 6-point stencil from Eq. (2) because this scheme and the default ITK scheme are not consistent. The figure shows that the error gets larger at areas where prescribed atrophy has discontinuous jumps.

360 images for the evaluation of such algorithms, users should compute Jacobian determinants using the same  
 361 numerical scheme as used by the atrophy estimation algorithm being evaluated. For instance, if multiple  
 362 time-steps was used in simulating the final image then the Jacobian must be computed at each individual  
 363 step and properly accumulated to get the final volume change.

### 364 4.3 Implementation of image warping

365 When implementing an algorithm to warp an image with a given deformation field, it is more convenient  
 366 to use the inverse of the deformation field. If  $\Phi_s$  is the output deformation field obtained from the brain  
 367 deformation model by using  $I_b$  as the input baseline image,  $\Phi_s$  maps any point  $\mathbf{x}$  in  $I_b$  to a point  $\mathbf{y}$  in the  
 368 simulated image  $I_s$  as follows:

$$\mathbf{y} = \Phi_s(\mathbf{x}).$$

369 However,  $\mathbf{y}$  is not guaranteed to be a discrete voxel location. Since we do not know the intensity values  
 370 of  $I_s$  *a priori* in the nearby discrete positions, the problem of interpolation is much more complex. Thus,  
 371 we start from a discrete voxel location  $\mathbf{y}$  in  $I_s$  where the value of intensity is to be found. Then, the  
 372 corresponding position  $\mathbf{x}$  in  $I_b$  can be obtained by using the inverse deformation field:

$$\mathbf{x} = \Phi_s^{-1}(\mathbf{y}).$$

373 If the transformed point  $\mathbf{x}$  is not a discrete point, we can interpolate the intensities of  $I_b$  from neighbouring  
 374 discrete locations. Let us denote the interpolation by square brackets. Thus  $i = I[\mathbf{x}]$  describes a mapping  
 375 of a point  $\mathbf{x}$  to an intensity,  $i$ , of the MR image  $I$  at  $\mathbf{x}$ . Using this notation, the intensity of the simulated

376 image at any position  $\mathbf{x}$  is given by:

$$I_b [\Phi_s^{-1}(\mathbf{x})].$$

377 The following option can be used to invert the deformation field:

```
378 --invert_field_to_warp #Invert u; default: do not invert
```

381 The implementation of the inversion is adapted from a fixed-point scheme implementation available in  
 382 ITK (Luethi, 2010). By default, the simulator uses B-spline interpolation of order three to warp the input  
 383 images.

#### 384 4.4 Standalone utility tools and scripts for pre-processing and post-processing

385 There are some standalone tools and scripts available for various pre-processing and post-processing  
 386 operations that are detailed in the documentation of the released software.

387 Some of these tools for pre-processing and post-processing operations are C++ executables based on ITK,  
 388 while others are python scripts. In this work, all the input segmentation of the model were obtained by using  
 389 FreeSurfer. As explained in Khanal et al. (2016b), these segmentation maps were processed to obtain in the  
 390 format required by the model. Although the provided scripts are developed for FreeSurfer segmentation  
 391 maps, they can be easily modified to adapt to other pre-processing tools. Finally, the registration and  
 392 simulation deformations were composed using `ComposeMultiTransform` of Advanced Neuroimaging  
 393 Tools (ANTs) (Avants et al., 2011).

394 The core component of `Simul@trophY` is the implementation of the brain deformation model.  
 395 Resampling of the intensity is straightforward once the deformations from the model and from registration  
 396 are available. The simulator is not dependent on any one particular registration algorithm. Although we  
 397 used LCC-LogDemons for illustrative purposes, this can be replaced with any other non-rigid registration  
 398 algorithms. Similarly pre-processing is also independent of `Simul@trophY`. We used FreeSurfer in the  
 399 simulation examples shown in this work, but any other skull stripping and segmentation algorithms can be  
 400 used. `Simul@trophY` provides some example scripts and some utility scripts, which could be modified  
 401 when using other tools for the pre-processing step.

## 5 DISCUSSION

402 In Khanal et al. (2016b), we presented a method to generate a subject-specific atrophy pattern by first  
 403 measuring the atrophy from the available time-points, and then simulating a new time-point by prescribing  
 404 the measured atrophy. In Khanal et al. (2016c), we extended the method to interpolate an unavailable  
 405 intermediate time-point MRI. In this work, we added realistic variation in the intensity of the synthetic  
 406 images. This fills an important gap in the existing literature to simulate atrophy in longitudinal images with  
 407 realistic intensity variation without explicitly modeling the noise and acquisition artefacts. The simulation  
 408 examples were shown using three types of atrophy patterns: i) very simple uniform volume changes in  
 409 small number of regions, ii) uniform atrophy in large number of regions, and iii) smoothly varying atrophy  
 410 patterns.

411 For each subject, we could generate large number of synthetic images by perturbing these atrophy patterns  
 412 in different ways. Even with the same atrophy pattern, we can generate multiple sets of longitudinal  
 413 sequences of varying intensity characteristics using the approach illustrated in Figure 4. Thus, by changing  
 414 the atrophy patterns and the image intensities, `Simul@trophY` could be used to generate a database of

415 very large number of simulated images. Such a database might be useful for training of machine learning  
416 algorithms.

417 In Figure 6, smoothly varying atrophy pattern was prescribed by taking the negative of the divergence of  
418 a stationary velocity field obtained by registering the input baseline image with a follow-up image of the  
419 same subject. The objective of the experiment was to illustrate the ability of *Simul@tropy* to simulate  
420 smoothly varying patterns of atrophy in addition to the piecewise continuous atrophy maps. Registration  
421 was taken just as a means of getting a realistic smoothly varying atrophy maps; it is worth mentioning that  
422 simulating the deformation to be close to the deformation obtained from the registration algorithm was not  
423 the objective of this experiment. This is because the actual deformation field depends on the regularization  
424 used in the registration algorithm which does not necessarily follow the modeling assumptions used by  
425 *Simul@tropy*.

426 Although the proposed method of resampling intensity from an image different from the input image  
427 provides more realistic variations, there are nevertheless certain issues one needs to be aware of. Since the  
428 simulated image has its intensities interpolated from another image, it can slightly reduce the noise variance.  
429 A neighbourhood with expansion in the simulated image have intensities with slightly different linear  
430 combinations of intensities coming from a smaller set of voxels in the input image. Thus, the simulated  
431 image would have a smoother autocorrelation in the neighbourhood compared to an equivalent real image.  
432 The fact that the simulated image has undergone interpolation and draws intensities from a limited set of  
433 raw voxels means that it is inherently smoother than the real scans. Finally, the usual spatial patterns of  
434 artifacts on real scans might not be exactly reproduced when warping real images. Any application using  
435 the simulated sets of images with the proposed approach should be aware of and ideally take into account  
436 these issues when interpreting results.

437 Use of repeat baseline scans to obtain intensity variation in the simulated images provides a very simple  
438 approach without using explicit noise and artifact models. One limitation with this is that the repeat baseline  
439 scans are not always available. When repeat scans are not available, we have proposed to use images at  
440 other time-points of the same subject, which requires performing non-linear registration. However, none  
441 of the non-linear registration methods are perfect and therefore the inaccuracies in registration affect the  
442 simulation results. This issue was discussed with illustrative examples in Section 4.1.

443 *Simul@tropy* can be used in evaluating atrophy estimation algorithms in similar ways as done by  
444 Pieperhoff et al. (2008); Camara et al. (2008); Sharma et al. (2010). Since the proposed approach to  
445 simulate images may need deformations estimated from image registration, the use of these simulated  
446 images for the evaluation of some registration algorithms can bring an issue of circularity. This limitation  
447 adds to another limitation present in all publications related to atrophy simulation that we are aware of:  
448 namely, the models used in simulating images could favour certain kinds of registration algorithms over  
449 others. Although the ground truth atrophy can be measured from the combined deformation fields, the  
450 users must be aware of both limitations when they use *Simul@tropy* for the evaluation of registration  
451 algorithms.

452 The ability to prescribe atrophy at any time point allows the user to introduce volume changes at different  
453 regions of the brain at different times. Thus, another interesting application of the simulator is to train  
454 and/or validate disease progression models such as the models proposed in Chen et al. (2012); Fonteijn  
455 et al. (2012); Jedynek et al. (2012); Dukart et al. (2013); Schmidt-Richberg et al. (2016). Having a database  
456 of longitudinal MRIs with known spatio-temporal distribution of atrophy can be useful to validate such

457 algorithms. Furthermore, since the algorithms use a data driven approach, the simulator could be useful to  
458 train or fine-tune such models.

459 Another possible application is in filling up unavailable time-point MRIs of some of the subjects, when  
460 performing group-wise longitudinal analysis. In such studies, usually the available time-point images of  
461 each subject are used to estimate subject-specific volume changes. These subject-specific measurements  
462 are then used to perform group-wise statistics to check whether there are significant differences amongst  
463 different groups in some particular regions of the brain. Databases used in such analyses, might not always  
464 have all the required time-point images for all the subjects. This could lead to bias if all the subjects are not  
465 aligned properly in the temporal dimension of disease progression. Simulating new time-point images for  
466 some subjects and using them in the analysis might allow evaluating the impact of such mis-alignments.

467 `Simul@tropy` could also be used in studying the role of morphology and intensity on atrophy  
468 estimation algorithms, and in machine learning based AD classification algorithms. `Simul@tropy`  
469 enables to perform such studies as it allows creating a large number of images by simulating atrophy  
470 patterns commonly observed in AD patients but with intensities taken from normal subjects and vice versa.

471 We hope to promote two directions of research in the community with open-source release of  
472 `Simul@tropy`. *First*, the public availability of `Simul@tropy` enables researchers to build their own  
473 simulated databases as needed. This might also hopefully lead to a large public database of ground truth  
474 simulated images, that could be used for benchmarking and evaluation of various image based morphometry  
475 tools. *Second*, we hope that `Simul@tropy` allows other researchers to build upon the biophysical model  
476 we presented in Khanal et al. (2016b), and investigate further, providing more accurate models of brain  
477 atrophy.

478 Finally, `Simul@tropy` is general enough to be used for other imaging modalities such as CT scans.  
479 It could also be used with images of any other organs, where one requires simulating specified volume  
480 changes. In this case, the pre-processing should be changed accordingly to generate a segmentation image  
481 and atrophy maps. Thus, once the software is public, other researchers might find it useful in applications  
482 that we have not foreseen yet.

## 6 CONCLUSIONS

483 We proposed a simulation framework that can generate realistic longitudinal MRIs with specified volume  
484 changes. The framework allows generating large number of subject-specific multiple time-point images  
485 based on a biophysical model of brain deformation due to atrophy. We developed an open-source software  
486 `Simul@tropy` to implement the proposed framework. The core part of `Simul@tropy` is the  
487 implementation of our brain deformation model presented in Khanal et al. (2016b). `Simul@tropy` is  
488 based on widely used state of the art libraries PETSc (for solving large systems of equations) and ITK (for  
489 medical image processing). Since the software is publicly available in an open-source repository, we hope  
490 that researchers can use it to create databases of ground truth images. The framework could be used to  
491 generate a common public database, which in turn could be used to validate and evaluate a large number  
492 of available atrophy estimation algorithms. Similarly, these databases could be valuable for data driven  
493 disease progression models including machine learning algorithms. Validation and training of the models  
494 that study temporal relationships, ordering and co-evolution of atrophy in different structures of the brain  
495 could be another interesting application.

## CONFLICT OF INTEREST STATEMENT

496 The authors declare that the research was conducted in the absence of any commercial or financial  
497 relationships that could be construed as a potential conflict of interest.

## FUNDING

498 Part of this work was funded by the European Research Council through the ERC Advanced Grant  
499 MedYMA 2011-291080.

## ACKNOWLEDGMENTS

500 1. We would like to thank Mehdi Hadj-Hamou for providing us registration results and the associated  
501 deformation fields that were used in this paper to resample intensity from different images. The  
502 preprocessing steps involved for this registration are explained in Hadj-Hamou et al. (2016).  
503 2. Most part of this work has first appeared in the PhD thesis of Bishesh Khanal (Khanal, 2016), and the  
504 working paper has been archived (Khanal et al., 2016a).  
505 3. Part of this work was funded by the European Research Council through the ERC Advanced Grant  
506 MedYMA 2011-291080.  
507 4. This work benefited from the use of the Insight Segmentation and Registration Toolkit (ITK), an open  
508 source software developed as an initiative of the U.S. National Library of Medicine and available at  
509 [www.itk.org](http://www.itk.org).  
510 5. The multi-platform configuration tool CMake was used for configuring ITK and facilitating its use from  
511 our project. CMake was partially funded by the U.S. National Library of Medicine as part of the Insight  
512 Toolkit project. CMake is an open source system and it is freely available at [www.cmake.org](http://www.cmake.org).

## SUPPLEMENTAL DATA

513 Supplementary Material should be uploaded separately on submission, if there are Supplementary Figures,  
514 please include the caption in the same file as the figure. LaTeX Supplementary Material templates can be  
515 found in the Frontiers LaTeX folder

## REFERENCES

- 516 Ashburner, J. (2013). Symmetric diffeomorphic modeling of longitudinal structural MRI. *Frontiers in*  
517 *Neuroscience* 6. doi:10.3389/fnins.2012.00197
- 518 Ashburner, J. and Friston, K. J. (2000). Voxel-based morphometry: the methods. *NeuroImage* 11, 805 – 821.  
519 doi:10.1006/nimg.2000.0582
- 520 Ashburner, J. and Ridgway, G. R. (2015). Tensor-based morphometry. In *Brain Mapping: An Encyclopedic*  
521 *Reference*, ed. A. W. Toga (Academic Press: Elsevier). 383–394. doi:10.1016/B978-0-12-397025-1.  
522 00309-2
- 523 Avants, B., Johnson, H. J., and Tustison, N. J. (2015). Neuroinformatics and the the insight toolkit.  
524 *Frontiers in Neuroinformatics* 9. doi:10.3389/fninf.2015.00005
- 525 Avants, B. B., Tustison, N. J., Song, G., Cook, P. A., Klein, A., and Gee, J. C. (2011). A reproducible  
526 evaluation of ants similarity metric performance in brain image registration. *NeuroImage* 54, 2033 –  
527 2044. doi:http://dx.doi.org/10.1016/j.neuroimage.2010.09.025



- 528 Balay, S., Brown, J., Buschelman, K., Gropp, W. D., Kaushik, D., Knepley, M. G., et al. (2013). PETSc  
529 Web page. [Http://www.mcs.anl.gov/petsc](http://www.mcs.anl.gov/petsc)
- 530 Camara, O., Schnabel, J. A., Ridgway, G. R., Crum, W. R., Douiri, A., Scahill, R. I., et al. (2008). Accuracy  
531 assessment of global and local atrophy measurement techniques with realistic simulated longitudinal  
532 alzheimer's disease images. *NeuroImage* 42, 696–709
- 533 Camara, O., Schweiger, M., Scahill, R. I., Crum, W. R., Sneller, B. I., Schnabel, J. A., et al. (2006).  
534 Phenomenological model of diffuse global and regional atrophy using finite-element methods. *IEEE*  
535 *Transactions on Medical Imaging* 25, 1417–30. doi:10.1109/TMI.2006.880588
- 536 Camara-Rey, O., Sneller, B. I., Ridgway, G. R., Garde, E., Fox, N. C., and Hill, D. L. (2006). Simulation  
537 of acquisition artefacts in mr scans: effects on automatic measures of brain atrophy. In *International*  
538 *Conference on Medical Image Computing and Computer-Assisted Intervention* (Springer), 272–280
- 539 Carmichael, O., McLaren, D. G., Tommet, D., Mungas, D., and Jones, R. N. (2013). Coevolution of brain  
540 structures in amnesic mild cognitive impairment. *NeuroImage* 66, 449–456. doi:10.1016/j.neuroimage.  
541 2012.10.029
- 542 Chen, R., Resnick, S. M., Davatzikos, C., and Herskovits, E. H. (2012). Dynamic bayesian network  
543 modeling for longitudinal brain morphometry. *NeuroImage* 59, 2330 – 2338. doi:http://dx.doi.org/10.  
544 1016/j.neuroimage.2011.09.023
- 545 Dukart, J., Kherif, F., Mueller, K., Adaszewski, S., Schroeter, M. L., Frackowiak, R. S. J., et al. (2013).  
546 Generative fdg-pet and mri model of aging and disease progression in alzheimer's disease. *PLoS Comput*  
547 *Biol* 9, 1–11. doi:10.1371/journal.pcbi.1002987
- 548 Fischl, B., Salat, D. H., Busa, E., Albert, M., Dieterich, M., Haselgrove, C., et al. (2002). Whole Brain  
549 Segmentation: Automated Labeling of Neuroanatomical Structures in the Human Brain. *Neuron* 33,  
550 341–355. doi:10.1016/S0896-6273(02)00569-X
- 551 Fonteijn, H. M., Modat, M., Clarkson, M. J., Barnes, J., Lehmann, M., Hobbs, N. Z., et al. (2012).  
552 An event-based model for disease progression and its application in familial Alzheimer's disease and  
553 Huntington's disease. *NeuroImage* 60, 1880–1889. doi:10.1016/j.neuroimage.2012.01.062
- 554 Freeborough, P. A. and Fox, N. C. (1997). The boundary shift integral: an accurate and robust measure  
555 of cerebral volume changes from registered repeat mri. *IEEE Transactions on Medical Imaging* 16,  
556 623–629. doi:10.1109/42.640753
- 557 Frisoni, G. B., Fox, N. C., Jack, C. R., Scheltens, P., and Thompson, P. M. (2010). The clinical use of  
558 structural MRI in Alzheimer disease. *Nature Reviews. Neurology* 6, 67–77. doi:10.1038/nrneurol.2009.  
559 215
- 560 Gorgolewski, K. J., Varoquaux, G., Rivera, G., Schwartz, Y., Ghosh, S. S., Maumet, C., et al. (2015).  
561 Neurovault.org: A web-based repository for collecting and sharing unthresholded statistical maps of the  
562 human brain. *Frontiers in Neuroinformatics* 9. doi:10.3389/fninf.2015.00008
- 563 Gudbjartsson, H. and Patz, S. (1995). The Rician Distribution of Noisy MRI Data. *Magnetic resonance*  
564 *in medicine : official journal of the Society of Magnetic Resonance in Medicine / Society of Magnetic*  
565 *Resonance in Medicine* 34, 910–914
- 566 Hadj-Hamou, M., Lorenzi, M., Ayache, N., and Pennec, X. (2016). Longitudinal analysis of image time  
567 series with diffeomorphic deformations: a computational framework based on stationary velocity fields.  
568 *Frontiers in Neuroscience* 10. doi:10.3389/fnins.2016.00236
- 569 Hua, X., Leow, A. D., Parikshak, N., Lee, S., Chiang, M.-C., Toga, A. W., et al. (2008). Tensor-based  
570 morphometry as a neuroimaging biomarker for alzheimer's disease: An {MRI} study of 676 ad, mci, and  
571 normal subjects. *NeuroImage* 43, 458 – 469. doi:http://dx.doi.org/10.1016/j.neuroimage.2008.07.013

- 572 Jedynak, B. M., Lang, A., Liu, B., Katz, E., Zhang, Y., Wyman, B. T., et al. (2012). A  
573 computational neurodegenerative disease progression score: Method and results with the alzheimer's  
574 disease neuroimaging initiative cohort. *NeuroImage* 63, 1478 – 1486. doi:http://dx.doi.org/10.1016/j.  
575 neuroimage.2012.07.059
- 576 Jenkinson, M. and Smith, S. (2001). A global optimisation method for robust affine registration of brain  
577 images. *Medical Image Analysis* 5, 143 – 156. doi:http://dx.doi.org/10.1016/S1361-8415(01)00036-6
- 578 Karaçali, B. and Davatzikos, C. (2006). Simulation of tissue atrophy using a topology preserving  
579 transformation model. *IEEE Transactions on Medical Imaging* 25, 649–52. doi:10.1109/TMI.2006.  
580 873221
- 581 Khanal, B. (2016). *Modeling and simulation of realistic longitudinal structural brain MRIs with atrophy in*  
582 *Alzheimer's disease*. theses, Université Nice Sophia Antipolis
- 583 Khanal, B., Ayache, N., and Pennec, X. (2016a). Simulating Realistic Synthetic Longitudinal Brain MRIs  
584 with known Volume Changes. Working paper or preprint
- 585 Khanal, B., Lorenzi, M., Ayache, N., and Pennec, X. (2014). A Biophysical Model of Shape Changes  
586 due to Atrophy in the Brain with Alzheimers Disease. In *Medical Image Computing and Computer-*  
587 *Assisted Intervention MICCAI 2014*, eds. P. Golland, N. Hata, C. Barillot, J. Hornegger, and R. Howe  
588 (Springer International Publishing), vol. 8674 of *Lecture Notes in Computer Science*. 41–48. doi:10.  
589 1007/978-3-319-10470-6\_6
- 590 Khanal, B., Lorenzi, M., Ayache, N., and Pennec, X. (2016b). A biophysical model of brain deformation  
591 to simulate and analyze longitudinal mris of patients with alzheimer's disease. *NeuroImage* 134, 35 – 52.  
592 doi:http://dx.doi.org/10.1016/j.neuroimage.2016.03.061
- 593 Khanal, B., Lorenzi, M., Ayache, N., and Pennec, X. (2016c). Simulating patient specific multiple  
594 time-point mris from a biophysical model of brain deformation in alzheimer's disease. In *Computational*  
595 *Biomechanics for Medicine: Imaging, Modeling and Computing*, eds. G. Joldes, B. Doyle, A. Wittek,  
596 P. M. F. Nielsen, and K. Miller (Springer International Publishing AG)
- 597 Koch, K., Reess, T. J., Rus, O. G., and Zimmer, C. (2016). Extensive learning is associated with gray  
598 matter changes in the right hippocampus. *NeuroImage* 125, 627 – 632. doi:http://dx.doi.org/10.1016/j.  
599 neuroimage.2015.10.056
- 600 Langlois, S., Desvignes, M., Constans, J. M., and Revenu, M. (1999). MRI geometric distortion: a simple  
601 approach to correcting the effects of non-linear gradient fields. *Journal of magnetic resonance imaging:*  
602 *JMRI* 9, 821–831
- 603 Lorenzi, M., Ayache, N., Frisoni, G., and Pennec, X. (2013). LCC-Demons: A robust and accurate  
604 symmetric diffeomorphic registration algorithm. *NeuroImage* 81, 470–483. doi:10.1016/j.neuroimage.  
605 2013.04.114
- 606 Luethi, M. (2010). Inverting deformation fields using a fixed point iteration scheme. *The Insight Journal*
- 607 Marcus, D. S., Fotenos, A. F., Csernansky, J. G., Morris, J. C., and Buckner, R. L. (2010). Open access  
608 series of imaging studies: Longitudinal MRI data in nondemented and demented older adults. *Journal of*  
609 *Cognitive Neuroscience* 22, 2677–2684
- 610 McCormick, M. M., Liu, X., Ibanez, L., Jomier, J., and Marion, C. (2014). Itk: Enabling reproducible  
611 research and open science. *Frontiers in Neuroinformatics* 8. doi:10.3389/fninf.2014.00013
- 612 Modat, M., Simpson, I. J. A., Cardoso, M. J., Cash, D. M., Toussaint, N., Fox, N. C., et al. (2014).  
613 Simulating neurodegeneration through longitudinal population analysis of structural and diffusion  
614 weighted mri data. In *Medical Image Computing and Computer-Assisted Intervention – MICCAI 2014:*  
615 *17th International Conference, Boston, MA, USA, September 14-18, 2014, Proceedings, Part III*, eds.

- 616 P. Golland, N. Hata, C. Barillot, J. Hornegger, and R. Howe (Springer International Publishing), Lecture  
617 Notes in Computer Science. 57–64. doi:10.1007/978-3-319-10443-0\_8
- 618 Pieperhoff, P., Südmeyer, M., Hömke, L., Zilles, K., Schnitzler, A., and Amunts, K. (2008). Detection  
619 of structural changes of the human brain in longitudinally acquired MR images by deformation field  
620 morphometry: methodological analysis, validation and application. *NeuroImage* 43, 269–87. doi:10.  
621 1016/j.neuroimage.2008.07.031
- 622 Prados, F., Cardoso, M. J., Leung, K. K., Cash, D. M., Modat, M., Fox, N. C., et al. (2015). Measuring  
623 brain atrophy with a generalized formulation of the boundary shift integral. *Neurobiology of aging* 36,  
624 S81–S90
- 625 Prakosa, A., Sermesant, M., Delingette, H., Marchesseau, S., Saloux, E., Allain, P., et al. (2013). Generation  
626 of synthetic but visually realistic time series of cardiac images combining a biophysical model and  
627 clinical images. *IEEE transactions on medical imaging* 32, 99–109. doi:10.1109/TMI.2012.2220375
- 628 Preboske, G. M., Gunter, J. L., Ward, C. P., and Jack, C. R. (2006). Common mri acquisition non-idealities  
629 significantly impact the output of the boundary shift integral method of measuring brain atrophy on  
630 serial mri. *Neuroimage* 30, 1196–1202
- 631 Radua, J., Canales-Rodriguez, E. J., Pomarol-Clotet, E., and Salvador, R. (2014). Validity of modulation  
632 and optimal settings for advanced voxel-based morphometry. *NeuroImage* 86, 81 – 90. doi:http:  
633 //dx.doi.org/10.1016/j.neuroimage.2013.07.084
- 634 Rosen, H. J., Gorno-Tempini, M. L., Goldman, W., Perry, R., Schuff, N., Weiner, M., et al. (2002). Patterns  
635 of brain atrophy in frontotemporal dementia and semantic dementia. *Neurology* 58, 198–208
- 636 Schmidt-Richberg, A., Ledig, C., Guerrero, R., Molina-Abril, H., Frangi, A., Rueckert, D., et al. (2016).  
637 Learning biomarker models for progression estimation of alzheimer’s disease. *PLoS ONE* 11, 1–27.  
638 doi:10.1371/journal.pone.0153040
- 639 Sepulcre, J., Sastre-Garriga, J., Cercignani, M., Ingle, G. T., Miller, D. H., and Thompson, A. J. (2006).  
640 Regional gray matter atrophy in early primary progressive multiple sclerosis: a voxel-based morphometry  
641 study. *Archives of neurology* 63, 1175–1180
- 642 Sharma, S., Noblet, V., Rousseau, F., Heitz, F., Rumbach, L., and Armspach, J. (2010). Evaluation of brain  
643 atrophy estimation algorithms using simulated ground-truth data. *Medical Image Analysis* 14, 373–89.  
644 doi:10.1016/j.media.2010.02.002
- 645 Sharma, S., Rousseau, F., Heitz, F., Rumbach, L., and Armspach, J. (2013). On the estimation and correction  
646 of bias in local atrophy estimations using example atrophy simulations. *Computerized Medical Imaging*  
647 *and Graphics* 37, 538 – 551. doi:http://dx.doi.org/10.1016/j.compmedimag.2013.07.002
- 648 Simmons, A., Tofts, P. S., Barker, G. J., and Arridge, S. R. (1994). Sources of intensity nonuniformity in  
649 spin echo images at 1.5 t. *Magnetic Resonance in Medicine* 32, 121–128
- 650 Sled, J. G., Zijdenbos, A. P., and Evans, A. C. (1998). A nonparametric method for automatic correction of  
651 intensity nonuniformity in MRI data. *IEEE transactions on medical imaging* 17, 87–97. doi:10.1109/42.  
652 668698
- 653 Smith, A. D. C., Crum, W. R., Hill, D. L., Thacker, N. A., and Bromiley, P. A. (2003). Biomechanical  
654 simulation of atrophy in MR images. In *Medical Imaging 2003* (International Society for Optics and  
655 Photonics), 481–490
- 656 Smith, S. M., Zhang, Y., Jenkinson, M., Chen, J., Matthews, P., Federico, A., et al. (2002). Accurate,  
657 robust, and automated longitudinal and cross-sectional brain change analysis. *Neuroimage* 17, 479–489
- 658 Whitwell, J. L. and Jack Jr, C. R. (2005). Comparisons between alzheimer disease, frontotemporal  
659 lobar degeneration, and normal aging with brain mapping. *Topics in Magnetic Resonance Imaging* 16,  
660 409–425

661 Wright, I., McGuire, P., Poline, J.-B., Travers, J., Murray, R., Frith, C., et al. (1995). A voxel-based method  
 662 for the statistical analysis of gray and white matter density applied to schizophrenia. *NeuroImage* 2, 244  
 663 – 252. doi:<http://dx.doi.org/10.1006/nimg.1995.1032>

## 7 APPENDIX

### 664 7.1 Running simul@tropy from command lines

665 Once the pre-processing steps described in Section 2.1 are performed and the desired atrophy map is  
 666 generated, these images can be used as input to the model by providing the following command line  
 667 arguments:

```
668 -atrophyFile           #Input atrophy map
669 -maskFile             #Input segmentation file
670 -imageFile            #Input image file
671
```

673 If the model parameters  $\mu$  and  $\lambda$  have uniform values in Label1 and Label2, they can be provided  
 674 as an argument to the option `-parameters`. On the other hand, if they need to have different values in  
 675 different parts of the brain, one needs to provide them as images similar to other input images as shown  
 676 below:

```
677 -parameters           # $\mu, \lambda$  in Region1, Region2. Format:  $\mu_1, \mu_2, \lambda_1, \lambda_2$ 
678 -muFile               #Ignore  $\mu$  from -parameters, use this image
679 -lambdaFile          #Ignore  $\lambda$  from -parameters, use this image
680 --useTensorLambda    # $\lambda$  given as DTI; default is scalar image
681
```

683 Some of the important options available are:

```
684 -boundary_condition  #dirichlet_at_walls or dirichlet_at_skull
685 --div12pt_stencil   #Use 12-point scheme; default: 6-point scheme
686 --relax_ic_in_csf   #Region1:  $\nabla \cdot \mathbf{u} + kp = 0$ ; default is  $\nabla \cdot \mathbf{u} = -a$ 
687 -relax_ic_coeff      #Value of  $k$ 
688 -numOfTimeSteps     #Number of time-steps to solve for
689
```

691 To solve the system of Eqs. (1), the argument to `-boundary_condition` should be  
 692 `dirichlet_at_skull` and `--relax_ic_in_csf` must be provided. Using `dirichlet_at_walls`  
 693 instead of `dirichlet_at_skull` will consider regions with `label0` in the same way as the regions  
 694 with `label2`, and sets the Dirichlet boundary conditions only at the image borders.

695 If `-numofTimeSteps` is greater than one, the simulator provides an output displacement field obtained  
 696 by composing output displacement fields of each time-steps. For any time-step  $n < \text{numOfTimeSteps}$ ,  
 697 it also provides output synthetic image by warping the input image with the displacement field obtained by  
 698 composing output displacement fields from time-step 1 to  $n$ . In addition to these outputs, if desired, some  
 699 other extra outputs can be generated as shown below:

```
700 -resPath              #Result path to store all the results
701 -resultsFileNamesPrefix #Prefix to be provided to all the images
702 --writePressure      #Write  $p$  as image to disk.
703
```

```
704 --writeForce           #Write  $(\mu + \lambda)\nabla a$  as image to disk.  
705  
706 --writeResidual       #Write solver residual as image to disk.
```

## FIGURES